



Multidimensional multiphysics simulations of the supercritical water-cooled fuel rod behaviors based on a new fuel performance code developed on the MOOSE platform

Zhouyu Liu ^{*}, Xiaobei Xu, Hongchun Wu, Liangzhi Cao

School of Nuclear Science and Technology, Xi'an Jiaotong University, Xi'an, Shaanxi 710049, China



ARTICLE INFO

Keywords:
Fuel performance
Multiphysics
MOOSE
SCWR
Flow blockage

ABSTRACT

Traditional nuclear fuel performance codes usually employ the operator split methods for multiphysics coupling and the quasi-two-dimensional approach (1.5D approach) for geometry modelling. However, the multiphysics behavior of the fuel element is often tightly coupled, and there exist some kinds of non-axisymmetric fuel elements in reactors. In this paper, a new fuel performance code named NECP-CALF has been developed based on the Multiphysics Object-Oriented Simulation Environment (MOOSE). It solves the multiphysics coupled equations using the JFNK method. A new geometrical approach called mixed dimensional approach is implemented in the new code, which allows users to model fuel elements with more flexibility. A UO₂-Zr fuel rod is simulated and the results are compared with BISON and CAMPUS to establish the proof-of-concept of this code. Then a small-scale UO₂-Zr fuel rod with azimuthally asymmetric cladding temperature is designed and simulated with the mixed dimensional approach to verify the accuracy and demonstrate the performance. Finally, the code is applied to the fuel performance simulation of a supercritical water-cooled fuel rod with flow blockage, and the results show the impact of the flow blockage on the fuel rod performance.

1. Introduction

The objective of nuclear fuel performance analysis is to predict the evolving behaviors of the nuclear fuel element, which is very important for fuel design and safety analysis (Van Uffelen et al., 2019). These evolving behaviors involve tightly-coupled multiphysics phenomena, including heat conduction, solid mechanics, gap heat transfer, swelling, densification, creep, fission gas release, etc (Williamson et al., 2012). In addition, although most fuel rods in reactors are axisymmetric, there exist some fuel rods in non-axisymmetric statuses, such as missing pellet surface defect, the eccentricity of the pellet, non-axisymmetric power and non-axisymmetric clad surface temperature, which requires multidimensional simulations (Van Uffelen et al., 2019).

Traditional fuel performance codes employ the quasi-two-dimensional approach (1.5D approach) (Berna et al., 1997) to model the fuel rod. In this approach, the fuel rod is divided into many layers along the axial direction, and one-dimensional representation is used in each layer. In addition to the approximation of geometry, the traditional codes usually utilize the operator split methods for the multiphysics coupling (Nakajima et al., 1994). For example, in the thermo-

mechanical coupling, the thermal equation is solved given fixed displacements of the pellet and cladding, and then the mechanical equation is solved based on the temperature gotten in the previous solution; this process is repeated until the temperature and the displacements are converged. The representatives of the traditional codes are FRAPCON (Berna et al., 1997), FEMAXI (Nakajima et al., 1994), TRANSURANUS (Lassmann, 1992) and ENIGMA (Jackson et al., 1990).

Although the traditional fuel performance codes have been widely applied to fuel design and safety analysis, there remain some problems. Firstly, the 1.5D approach cannot be applied to the non-axisymmetric fuel element. Secondly, the operator split methods may converge very slowly if the multiphysics system is tightly coupled, which may be aggravated when the coupled physics also operate on disparate time scales (Knoll et al., 2003; Ropp et al., 2004). Tighter multiphysics and multidimensional capabilities are needed to solve these two problems.

In fact, the requirement of these capabilities exists in many fields of numerical simulation besides the fuel performance analysis. Noticing this widespread issue, the Multiphysics Object-Oriented Simulation Environment (MOOSE) (Gaston et al., 2009) is developed by the Idaho National Laboratory (INL), which is a general and open-source

* Corresponding author at: 28 Xianning West Road, Xi'an, Shaanxi 710049, China.

E-mail address: zhouyuliuxjtu.edu.cn (Z. Liu).

numerical simulation platform for supporting the fast development of multiphysics multidimensional simulation codes. MOOSE discretizes the partial differential equations (PDEs) to a set of nonlinear algebraic equations through the finite-element method, enabling high geometric adaptability for modeling. Considering the complexity of the multiphysics coupling, MOOSE utilizes the Jacobian-free Newton-Krylov method (JFNK method) to solve the coupled set of nonlinear algebraic equations. Different from the operator split method in which each physics is solved one after another, the JFNK method solves all solution variables simultaneously using a strongly convergent nonlinear solver and an efficient linear solver. It will improve the convergence for the tightly coupled multiphysics system compared to the operator split methods (Knoll and Keyes, 2004; Mousseau and Knoll, 2006). There are also some other useful capabilities in MOOSE, such as automatically parallel, built-in mesh adaptivity and flexible graphical user interface. The representative of the MOOSE-based codes is BISON (Williamson et al., 2012) developed by INL, which is applicable to solving 1D, 2D axisymmetric and 3D fuel performance problems (Hales et al., 2016). In addition to the application to the traditional UO₂-Zr fuel (Spencer et al., 2016), BISON has been used to simulate the tristructural isotropic (TRISO) coated fuel (Hales et al., 2013), accident tolerant fuel (ATF) (Che et al., 2018), internally and externally cooled annular fuel (IXAF) and helical cruciform fuel (HCF) (Deng et al., 2019).

In this paper, a new fuel performance analysis code named NECP-CALF (Code for Analysis of nucLear Fuel developed by NECP laboratory) is developed based on the MOOSE platform. It solves the multiphysics coupled equations using the JFNK method. The geometrical models of fuel elements are based on the finite element method. Besides normal 1D, 2D and 3D models, a new modeling approach called the mixed dimensional approach is implemented in the new code. In this approach, a fuel element is divided into many layers along the axial direction, and users can freely choose the model in appropriate dimension, such as 1D or 2D, for each layer. It allows the users to model the fuel element combining efficiency and accuracy with more flexibility.

The SCWR (supercritical water-cooled reactor) is one of the six Generation IV reactors proposed by Generation IV International Forum (GIF). The main advantage of the SCWR is the improved economy due to the higher thermal efficiency and plant simplification (Ruzickova et al., 2015). In some SCWR designs, wire wrap spacer is used to enhance the coolant mixing flow and fix the fuel rods. However, the wire wrap detachment may block the coolant channels and cause non-axisymmetrically higher cladding temperatures, threatening the fuel element integrity (Liu et al., 2013). Liu studied this accident in the aspect of thermal-hydraulics (Liu et al., 2013). However, the fuel performance analysis for this accident has not been reported. In this work, a supercritical water-cooled fuel rod under the accidental and normal conditions is simulated using the new code. The results are compared to show the impact of the flow blockage accident on the fuel rod performance.

This paper is organized as follows: Section 2 describes the multiphysics models adopted in this work, including the governing equations, gap heat transfer model, mechanical contact model, plenum/gap pressure model and material behavior models. Section 3 describes the geometrical models used in this study. In Section 4, a UO₂-Zr fuel rod is simulated, and the results are compared with BISON and CAMPUS (Liu et al., 2016) to establish the proof-of-concept of this code. In Section 5, a small-scale UO₂-Zr fuel rod with azimuthally asymmetric cladding temperature is simulated using the mixed dimensional approach to verify the new approach. In Section 6, the supercritical water-cooled fuel rod with flow blockage is simulated to study the impact of the accident on the fuel rod performance. Section 7 provides a summary of this work.

2. Multiphysics models

The fuel performance analysis involves many physical processes, including heat conduction, solid mechanics, gap heat transfer, swelling,

densification, creep, fission gas release, etc. The models adopted in this work are described in this section.

2.1. Governing equations

The main task of the fuel performance simulation is to solve the coupled thermomechanical equations. The thermal behavior of the fuel element is prescribed using the heat conduction equation

$$\rho C_p \frac{\partial T}{\partial t} + \nabla(-k\nabla T) - S = 0 \quad (1)$$

where ρ is the density, C_p is the specific heat, T is the temperature, k is the thermal conductivity and S is the heat source (generated by the nuclear fission).

It is assumed that the pellet and the clad keep in the quasistatic status at each time increment. Thus, the mechanical behavior of the fuel element can be prescribed using Cauchy's equation

$$\nabla \cdot \sigma + \rho f = 0 \quad (2)$$

where σ is the Cauchy stress, ρ is the density and f is the body force per unit mass.

The solvers for these two equations are from the HeatConduction module and the TensorMechanics module in MOOSE.

2.2. Gap heat transfer model

The heat flux across the pellet-to-clad gap is given using Newton's law of cooling

$$q = h_{gap}(T_f - T_c) \quad (3)$$

where h_{gap} is the total conductance across the gap, T_f is the temperature at the fuel surface, T_c is the temperature at the internal surface of the clad.

The total conductance is given by

$$h_{gap} = h_g + h_s + h_r \quad (4)$$

where h_g is the conductance due to gas heat transfer, h_s is the conductance due to solid-solid contact, h_r is the conductance due to thermal radiation.

The gas conductance is computed using the model proposed by Ross and Stoute (1962)

$$h_g = \frac{k_g}{d_g + C_r(r_f + r_c) + g_f + g_c} \quad (5)$$

where k_g is the thermal conductivity of the gas, d_g is the gap width, C_r is a roughness coefficient, r_f is the roughness of the pellet surface, r_c is the roughness of the internal surface of the clad, g_f is the jump distance at the fuel surface, g_c is the jump distance at the inner surface of the clad.

The gap of the LWR fuel element is initially filled with He. With the burnup increasing, however, the fission gas (mainly Xe and Kr) will be released into the gap, reducing the thermal conductivity of the gas.

The thermal conductivity of the gas mixtures is computed using the formulation from MATPRO (Allison et al., 1993)

$$k_g = \sum_{i=1}^n \left(\frac{k_i x_i}{x_i + \sum_{j=1}^n (1 - \delta_{ij}) \psi_{ij} x_j} \right) \quad (6)$$

$$\psi_{ij} = \phi_{ij} \left(1 + 2.41 \frac{(M_i - M_j)(M_i - 0.142M_j)}{(M_i + M_j)^2} \right) \quad (7)$$

$$\phi_{ij} = \frac{\left[1 + \left(\frac{k_i}{k_j}\right)^{\frac{1}{2}} \left(\frac{M_i}{M_j}\right)^{\frac{1}{4}}\right]^2}{2^{\frac{3}{2}} \left(1 + \frac{M_i}{M_j}\right)^{\frac{1}{2}}} \quad (8)$$

where k_g is the thermal conductivity of the gas mixtures ($\text{Wm}^{-1}\text{K}^{-1}$), δ_{ij} is the Kronecker Delta, n is the number of components in mixture, M_i is the molecular weight of component i , x_i is the mole fraction of the component i , k_i is the thermal conductivity of the component i ($\text{Wm}^{-1}\text{K}^{-1}$).

The roughness coefficient is computed using the formulation from reference (Lanning and Hann, 1975)

$$C_r = 2e^{-0.00125P} \quad (9)$$

where P is the contact pressure between the fuel and the clad (kgf/cm^2).

The conductance due to solid-solid contact is computed using the empirical model suggested by Ross and Stoute (Ross and Stoute, 1962)

$$h_s = C_s \frac{2k_f k_c P_{contact}}{(k_f + k_c)\sqrt{\delta H}} \quad (10)$$

where C_s is an empirical constant recommended as 10, k_f is the thermal conductivity of the fuel, k_c is the thermal conductivity of the clad, $P_{contact}$ is the contact pressure between the fuel and the clad, δ is the average gas film thickness, H is the Meyer hardness of the softer material (usually the clad).

The conductance due to thermal radiation can be derived using the Stefan-Boltzmann law

$$h_r = \frac{\sigma F_e (T_f^4 - T_c^4)}{(T_f - T_c)} = \sigma F_e (T_f^2 + T_c^2)(T_f + T_c) \quad (11)$$

where σ is the Stefan-Boltzmann constant, F_e is an emissivity function, T_f is the temperature of the fuel surface, T_c is the temperature of the internal surface of the clad. Since the gap width is very small compared to the radius of the fuel element, the fuel surface and the clad surface can be considered to be infinite-parallel. Thus, the emissivity function can be defined as

$$F_e = \frac{1}{\varepsilon_f^{-1} + \varepsilon_c^{-1} - 1} \quad (12)$$

where ε_f and ε_c are the emissivity of the fuel surface and the clad surface.

2.3. Mechanical contact model

A built-in mechanical contact model in MOOSE is adopted in this work, which is based on three requirements

$$g \leq 0 \quad (13)$$

$$t_N \geq 0 \quad (14)$$

$$t_N g = 0 \quad (15)$$

where g is the penetration distance between the two surfaces, t_N is the contact force opposing penetration. The detail of this model can be seen in reference (Hales et al., 2016).

2.4. Plenum/gap pressure model

The pressure in the plenum and the gap is computed based on the ideal gas law

$$P = \frac{nR\bar{T}}{V} \quad (16)$$

where n is the moles of the gas, R is the ideal gas constant, \bar{T} is the

average temperature of the gas and V is the volume of the cavity. The moles of the gas at any time is the sum of the amount of the initial gas (usually He for the LWR fuel element) and the amount of the fission gas (mainly Xe and Kr for UO_2 fuel) released into the cavity with the burnup increasing. The average temperature of the gas is computed using the volume-weighted average method (Hales et al., 2016)

$$\bar{T} = \frac{\int T dV}{\int dV} \quad (17)$$

where \bar{T} is the average temperature of the gas, T is the temperature at a point in the gap/plenum and V is the volume occupied by the gas. It can be assumed that a differential volume is equal to a varying distance times a differential area

$$dV = \delta dA \quad (18)$$

where dV is the differential volume, dA is the differential area of the fuel or cladding surface, δ is the gap width between the fuel and cladding surface. The temperature at a point in the gap/plenum can be approximated as

$$T = \frac{T_f + T_c}{2} \quad (19)$$

where T_f is the temperature at the fuel surface and T_c is the temperature at the cladding surface. Then the average temperature of the gas can be written as

$$\bar{T} = \frac{\int_A \frac{T_f + T_c}{2} \delta dA}{\int_A \delta dA} \quad (20)$$

where A is the total surface of the fuel or cladding.

2.5. UO_2 models

UO_2 is the most commonly-used fuel material for the LWR fuel element. The models describing the important material behaviors such as temperature and burnup dependent thermal properties, swelling, densification, creep and fission gas release are presented in this section.

2.5.1. Thermal properties

The thermal conductivity of UO_2 is computed using the Fink-Lucuta model (Fink et al., 1981; Lucuta et al., 1996)

$$k = k_{100} f_d f_p f_{por} f_r \quad (21)$$

$$k_{100} = k_{95} \left(\frac{1}{1 - 0.05(2.6 - 0.5T_n)} \right) \quad (22)$$

$$k_{95} = \frac{100}{7.5408 + 17.692T_n + 3.6142T_n^2} + \frac{6400}{T_n^{2.5}} \exp\left(-\frac{16.35}{T_n}\right) \quad (23)$$

$$f_d = \left(\frac{1.09}{bu^{3.265}} + 0.0643\sqrt{\frac{T}{bu}} \right) \arctan\left(\left(\frac{1.09}{bu^{3.265}} + 0.0643\sqrt{\frac{T}{bu}} \right)^{-1} \right) \quad (24)$$

$$f_p = 1.0 + \left(\frac{0.019bu}{3.0 - 0.019bu} \right) (1.0 + \exp(-0.01(T - 1200)))^{-1} \quad (25)$$

$$f_{por} = \frac{1.0 - p}{1.0 + 0.5p} \quad (26)$$

$$f_r = 1 - \frac{0.2}{1 + \exp\left(\frac{T - 900}{80}\right)} \quad (27)$$

where k is the thermal conductivity of UO_2 ($\text{Wm}^{-1}\text{K}^{-1}$), k_{100} is the thermal conductivity of 100%-theoretical-density UO_2 ($\text{Wm}^{-1}\text{K}^{-1}$), f_d is

the dissolved fission products correction, f_p is the precipitated fission products correction, f_{por} is the porosity correction, f_r is the radiation damage correction, k_{95} is the thermal conductivity of 95%-theoretical-density UO_2 ($\text{Wm}^{-1}\text{K}^{-1}$), T_n is the temperature divided by 1000 (K), bu is the burnup (at.%), T is the temperature (K), p is the porosity.

The specific heat of UO_2 is computed using the model from MATPRO (Allison et al., 1993)

$$C_p = \frac{K_1 \theta^2 \exp\left(\frac{\theta}{T}\right)}{T^2 \left[\exp\left(\frac{\theta}{T}\right) - 1 \right]^2} + K_2 T + \frac{2K_3 E_D}{2RT^2} \exp\left(\frac{-E_D}{RT}\right) \quad (28)$$

where C_p is the specific heat of UO_2 ($\text{Jkg}^{-1}\text{K}^{-1}$), K_1 is 296.7, θ is 535.285, T is the temperature (K), K_2 is 2.43×10^{-2} , K_3 is 8.745×10^7 , E_D is 1.577×10^5 , R is the ideal gas constant.

2.5.2. Densification

At the early stage of the fuel life, the high pressure under the high temperature and radiation will reduce the porosity, causing the shrink of the fuel. This phenomenon is called “densification”. It is computed using the ESCORE empirical model (Rashid et al., December 2004)

$$\epsilon_D = \Delta\rho_0 \left(\exp\left(\frac{Bu_n(0.01)}{C_D Bu_D}\right) - 1 \right) \quad (29)$$

$$C_D = \begin{cases} 7.235 - 0.0086(T - 25) & T < 750 \\ 1 & T \geq 750 \end{cases} \quad (30)$$

where ϵ_D is the densification strain, $\Delta\rho_0$ is the total densification that can occur, Bu is the burnup, Bu_D is the burnup at which densification is complete, T is the temperature (°C).

2.5.3. Swelling

Due to the accumulation of the fission products, the fuel pellet will expand as the burnup increases, causing the reduction of the gap width and even the pellet-clad mechanical interaction. This phenomenon, called “swelling”, is modeled by the formulation from MATPRO (Allison et al., 1993)

$$\Delta\epsilon_{sw-s} = 5.577 \times 10^{-5} \rho \Delta Bu \quad (31)$$

$$\Delta\epsilon_{sw-g} = 1.96 \times 10^{-31} \rho \Delta Bu (2800 - T)^{11.73} \times \exp(-0.0162(2800 - T) - 0.0178 \rho Bu) \quad (32)$$

where $\Delta\epsilon_{sw-s}$ is the volumetric solid swelling increment, ρ is the density (kgm^{-3}), ΔBu is the burnup increment (fissions/atoms-U), $\Delta\epsilon_{sw-g}$ is the volumetric gaseous swelling increment, T is the temperature (K), Bu is the burnup (fissions/atoms-U).

2.5.4. Cracking

The high power in the fuel pellet will establish a significant temperature gradient from center to edge, which may cause high thermal stress and then induce cracking in the fuel. Those cracks will change the structure of the fuel pellet and increase the effective fuel volume. A built-in smeared cracking model in MOOSE is adopted in this work, simulating the cracking by adjusting the elastic constants at material points. In this model, critical stress will be set to determine whether the material is cracked. When the principal stress of exceeds the critical stress of the material at a point, the material is considered cracked at that point and the stress is reduced to zero. The detail of this model can be seen in reference (Rashid, 1974).

2.5.5. Thermal and irradiation creep

The combined secondary thermal creep and irradiation creep of UO_2 is computed using the MATPRO FCREEP material model (Allison et al.,

1993)

$$\dot{\epsilon} = \frac{A_1 + A_2 \dot{F}}{(A_3 + D)G^2} \sigma e^{\frac{-Q_1}{RT}} + \frac{A_4}{A_6 + D} \sigma^{4.5} e^{\frac{-Q_2}{RT}} + A_7 \dot{F} \sigma e^{\frac{-Q_3}{RT}} \quad (33)$$

where $\dot{\epsilon}$ is the creep rate (1/s), A_1 is 0.3919 , A_2 is 1.31×10^{-19} , \dot{F} is the volumetric fission rate ($\text{m}^{-3}\text{s}^{-1}$), A_3 is -87.7 , D is the fuel density (in percent of theoretical), G is the grain size (μm), σ is the effective Mises stress (Pa), Q_1 is 376591 J/mol, R is the ideal gas constant, T is the temperature (K), A_4 is 2.0391×10^{-25} , A_6 is -90.5 , Q_2 is 552334 J/mol, A_7 is 3.7226×10^{-35} , Q_3 is 21759 J/mol.

2.5.6. Fission gas behavior

The fission gas released from the fuel pellet to the gap substantially impacts on the fuel element behaviors. Firstly, the thermal conductivity of the fission gas (mainly Xe, Kr) is lower than He, causing the aggravation of gap heat transfer and then the increase of the fuel temperature. Secondly, the fission gas will raise the gap pressure, obstructing the reduction of the gap width.

The Forsberg-Massih two-stage model (Forsberg and Massih, 1985a) is adopted in this work to describe fission gas behavior. The fission gas is produced in the fuel grains; driven by the concentration gradient, the fission gas diffuses to the fuel grain boundaries, forming the intergranular gas bubbles. At the second stage, the accumulation of the fission gas at the boundaries causes the bubble growth, coalescence and interconnection, eventually forming a tunnel network through which the fission gas at the boundaries can be released to the gap and the plenum.

The diffusion process at the first stage can be described using the following equation:

$$\frac{\partial C_g}{\partial t} = D_{eff} \frac{1}{r^2} \frac{\partial}{\partial r} \left(r^2 \frac{\partial C_g}{\partial r} \right) + \beta \quad (34)$$

where C_g is the intragranular gas concentration (m^{-3}), t is the time (s), D_{eff} is the effective gas diffusion coefficient (m^2s^{-1}), r is the radial coordinate in the spherical grain (m), β is the gas generation rate ($\text{m}^{-3}\text{s}^{-1}$).

Many algorithms can be used to solve the diffusion equation, such as ANS-5.4 (Rausch and Panisko, 1979), URGAS (Elton and Lassmann, 1987; Lassmann and Benk, 2000), FORMAS (Lassmann and Benk, 2000; Forsberg and Massih, 1985b; Hermansson and Massih, 2002) and PolyPole-1 (Pizzocri et al., 2016). In this work, the PolyPole-1 algorithm is adopted, which is a semi-analytical algorithm that can achieve accuracy and efficiency. It is based on the analytic modal solution of the diffusion equation for constant conditions, combined with polynomial corrective terms that embody the information on the deviation from constant conditions (Pizzocri et al., 2016). The detail of this model can be seen in reference (Pizzocri et al., 2016).

In the second stage, the fission gas accumulates in the fuel grain boundaries until the tunnel network is formed. The formation of the tunnel network is a very complex physical process. In this work, it is simplified by assuming a grain boundary saturation for the fission gas. If the area density of the fission gas exceeds the saturation, the tunnel network is considered formed and the extra fission gas is released to the gap. The grain boundary saturation is computed using the model from reference (White and Tucker, 1983)

$$N_s = \frac{4rf(\theta)V_c}{3k_B T \sin^2 \theta} \left(\frac{2\gamma}{r} + P_{ext} \right) \quad (35)$$

$$f(\theta) = 1 - 1.5 \cos \theta + 0.5 \cos^3 \theta \quad (36)$$

where N_s is the grain boundary saturation (atoms/m²), r is the grain boundary bubble radius (m), $f(\theta)$ is a correction that accounts for the shape of the bubble, V_c is the grain boundary bubble fraction at saturation, k_B is the Boltzmann constant, T is the temperature (K), θ is the semi-dihibited angle between bubble surfaces (°), γ is the bubble surface tension (J/m²), P_{ext} is the externally applied hydrostatic pressure (Pa).

2.6. Zircaloy models

Zircaloy is the most commonly-used clad material for the LWR fuel element. The thermal creep, irradiation creep and Meyer hardness of Zircaloy are described in this section.

2.6.1. Thermal creep

The thermal creep of Zircaloy is computed using the model proposed by Hayes and Kassner (2006)

$$\dot{\epsilon}_{th} = A_0 \left(\frac{\sigma_m}{G} \right)^n e^{\frac{Q}{RT}} \quad (37)$$

where $\dot{\epsilon}_{th}$ is the effective thermal creep rate (s^{-1}), A_0 is $3.14 \times 10^{24} s^{-1}$, σ_m is the effective Mises stress (Pa), G is the shear modulus (Pa), n is 5, Q is the activation energy (J/mol), R is the universal gas constant (Jmol $^{-1}$ K $^{-1}$), T is the temperature (K).

2.6.2. Irradiation creep

The irradiation creep of Zircaloy is computed using the model proposed by Hoppe (1991)

$$\dot{\epsilon}_{ir} = C_0 \Phi^{C_1} \sigma_m^{C_2} \quad (38)$$

where $\dot{\epsilon}_{ir}$ is the effective irradiation creep rate (1/s), C_0 is 2.846×10^{-24} for ZIRLO, Φ is the fast neutron flux ($n/m^2 s$), C_1 is 0.85, σ_m is the effective Mises stress (Pa), C_2 is 1.0.

2.6.3. Meyer hardness

In the gap heat transfer model, Meyer hardness of the soft material (usually the clad) is required to compute the solid–solid conductance. As the contact pressure between the two surfaces increases, the contact enlarges points due to localized plastic deformation, and the solid-to-solid thermal conductance is improved (Luscher et al., 2010). The data of the Meyer hardness of Zircaloy are from reference (Luscher et al., 2010), as shown in Table 1.

2.7. SS316 models

Stainless steel 316 (SS316) is an austenitic chromium-nickel stainless steel containing a deliberate amount of molybdenum which increases general corrosion resistance and significantly improves its pitting resistance to chloride ion solutions. The molybdenum addition also provides increased strength at elevated temperatures. It can be used in SCWRs as cladding material (Maráczy et al., 2015). For SCWR fuel performance simulations, models of SS316 are implemented in NECP-CALF, which are described in this section.

2.7.1. Thermal properties

The thermal conductivity of SS316 is computed using the model from reference (Mills and Values, 2002)

$$k = -7.301 \times 10^{-6} T^2 + 2.716 \times 10^{-2} T + 6.308 \quad (39)$$

where k is the thermal conductivity ($Wm^{-1}K^{-1}$), T is the temperature (K).

Specific heat of SS316 is computed using the model from reference (Mills and Values, 2002)

$$C_p = 428.46 + 0.1816 T \quad (40)$$

where C_p is the specific heat ($Jkg^{-1}K^{-1}$), T is the temperature (K).

Table 1
Meyer hardness of zircaloy.

| Temperature/K | 293 | 335 | 389 | 460 | 588 | 678 | 778 | 871 |
|---------------|------|----------|----------|---------|---------|---------|---------|---------|
| Hardness/MPa | 2000 | 1474.576 | 1135.593 | 892.655 | 689.266 | 570.621 | 384.181 | 203.390 |

The Meyer hardness at the temperatures not listed in the table can be obtained through interpolation.

2.7.2. Elasticity

Young's modulus of SS316 is computed using the model from reference (Hales et al., 2016)

$$E = 2.15946 \times 10^{11} - 7.07727 \times 10^7 T \quad (41)$$

where E is the Young's modulus, T is the temperature (K).

Poisson's ratio is a constant from reference (Hales et al., 2016)

$$\nu = 0.31 \quad (42)$$

where ν is the Poisson's ratio.

2.7.3. Thermal expansion

The mean linear thermal expansion coefficient of SS316 is computed using the formulation from reference (Mills and Values, 2002)

$$\bar{\alpha}(T) = (16 + 6 \times 10^{-3} T) \times 10^{-6} \quad (43)$$

where $\bar{\alpha}$ is the mean linear thermal expansion coefficient (K^{-1}), T is the temperature ($^{\circ}C$), the reference temperature is $25^{\circ}C$.

2.7.4. Thermal creep

The thermal creep of SS316 is computed using the model from reference (Altenbach and Gorash, 2013)

$$\dot{\epsilon}_{cr} = a \cdot \exp\left(\frac{-Q_{ln}}{RT}\right) \cdot \sinh\left[b \cdot \exp\left(\frac{-Q_{pw}}{RT}\right) \sigma\right] \quad (44)$$

where $\dot{\epsilon}_{cr}$ is the effective creep rate (1/h), a is $75776 h^{-1}$, Q_{ln} is 170000 J/mol, R is the universal gas constant, T is the temperature ($^{\circ}C$), b is 0.7 MPa $^{-1}$, Q_{pw} is 12000 J/mol, σ is the effective Mises stress (MPa).

The SS316 models are used in the SCWR-FQT flow blockage simulation. The flow blockage will induce extremely higher cladding temperature, causing the thermal creep of the cladding to be significantly larger than the irradiation creep. So, the irradiation creep of SS316 is ignored here.

2.7.5. Plasticity

A power-law equation can describe the Strain-stress correlation of SS316 in plasticity from reference (Desu et al., 2016), and it is simplified to a linear hardening model to reduce the nonlinearity.

$$\sigma = \sigma_s + H(\varepsilon - \varepsilon_s) \quad (45)$$

where σ is the stress (MPa), $\sigma_s = 200$ MPa is the yield strength, $H = 1600$ MPa is the hardening constant, ε is the strain, ε_s is the strain at the beginning of yield.

3. Geometrical models

NECP-CALF is based on the MOOSE platform, which supports 1D, 2D and 3D models. The models can be generated by the finite-element modeling software such as Gmesh, SALOME, CUBIT and ICEM-CFD.

Besides, a new geometrical approach called the mixed dimensional method is developed in NECP-CALF. It can be regarded as an extension of the 1.5D model. It is suitable for the fuel element, which both has the axisymmetric region and the non-axisymmetric region along the axial direction. The procedures of this approach are:

- (1) Divide the fuel element into an appropriate number of axial layers depending on the variance of the conditions along the axial direction (power, cladding temperature, etc.).
- (2) Employ the model with the appropriate dimension for each layer. For example, if the layer is axisymmetric, a 1D model could be applied; if the layer is non-axisymmetric, a 2D model should be used.

Different axial layers are supposed to be independent and coupled only through the plenum gas in this approach. After modeling the fuel element, the procedures of the computation in a single time step are:

- (1) Execute the fuel performance simulations for each layer. If it is the first iteration, the parameters of the gap gas (temperature, pressure and released fission gas) are from the last time step.
- (2) Update the parameters of the gap gas depending on the results of the simulations for each layer. The gap gas parameters will be transferred into each layer.
- (3) Repeat (1) and (2) until the solutions are converged.

Fig. 1 is the schematic of the mixed dimensional approach.

The simulations for each layer are implemented based on a Moose-Object called MultiApp (Gaston, 2015; Martineau, 2020), which allows the execution of multiple MOOSE applications simultaneously and the coupling of different MOOSE applications. For example, when 1D and 2D models are used in the mixed dimensional approach, as shown in **Fig. 2**, a “Master” application is set up to compute the plenum gas parameters and control the executions of the MultiApps. Below the “Master” application, there are two MultiApps for the 1D and 2D fuel performance simulations, respectively. Each of the MultiApps has multiple Sub-apps, each of which simulates a single axial layer. At the beginning of the time step, the MultiApps are executed successively. Then the gap temperatures and the fission gas release of each layer are transferred to the “Master”. The “Master” computes the plenum gas parameters and transfers them back to the MultiApps. Then the Multi-Apps are executed based on the updated plenum gas parameters. These procedures are repeated until the solutions are converged.

4. UO₂-Zr fuel rod simulation

In this section, the results of a traditional PWR UO₂-Zr fuel rod simulation are presented, compared with the results of BISON

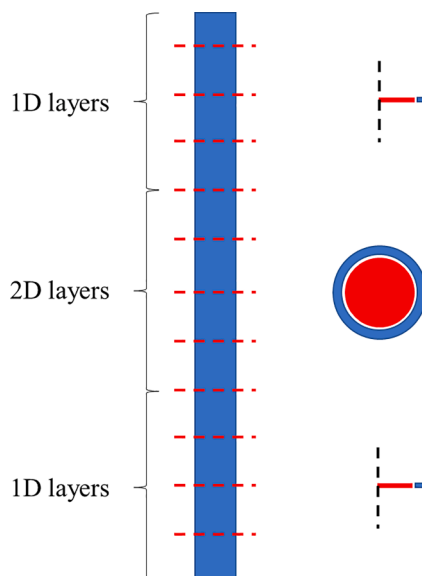


Fig. 1. Schematic of the mixed dimensional approach.

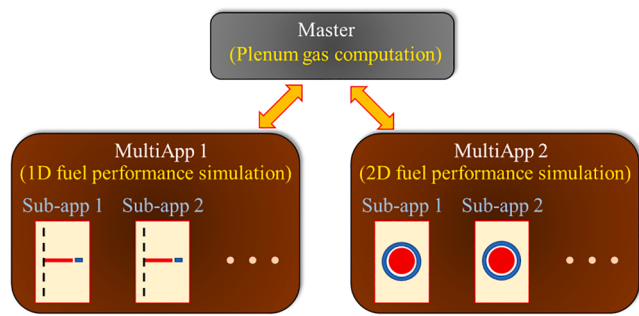


Fig. 2. Structure of the MultiApps for the mixed dimensional approach.

(Williamson et al., 2012) and CAMPUS (Liu et al., 2016). It should be noted that the results from the cited papers represent the code capabilities at that time (in 2012 for BISON; in 2016 for CAMPUS) but that the code and capabilities have changed since then because both of the codes are under development (Toptan et al., 2020; Liu et al., 2020). In addition, both NECP-CALF and BISON are based on MOOSE. However, The version of MOOSE used by BISON in the cited paper is released in 2012 and the version of MOOSE used by NECP-CALF here is released in 2018.

This problem is from reference (Williamson et al., 2012), which describes a simplified traditional PWR UO₂-Zr fuel rodlet. The radius of the pellet is 4.1 mm. The initial gap width is 80 μm, and the plenum gas is He with the initial pressure of 2 MPa. The thickness of the cladding is 0.57 mm. The length of a pellet is 11.9 mm, and the pellet stack consists of 10 pellets. The plenum to fuel length ratio is 0.045. A uniform convective boundary condition is set at the external surface of the cladding. The power history has two periods: in the beginning, the linear heating rate rises linearly from zero to 200 W/cm over 3 h; then, the power is held constant for 3.2 years. The Young's modulus, Poisson's ratio and thermal expansion coefficient for the fuel are 219 GPa, 0.345 and $10.0 \times 10^{-6} \text{K}^{-1}$ respectively (Olander 1990). The thermal conductivity, Young's modulus, Poisson's ratio and thermal expansion coefficient for the cladding are $16 \text{Wm}^{-1}\text{K}^{-1}$, 75 GPa, 0.3 and $5.0 \times 10^{-6} \text{K}^{-1}$, respectively (Allison et al., 1993). The fracture strength of the fuel is 130 MPa (H. Bailly, D. Ménessier, C. Prunier (Eds.), *The Nuclear Fuel of Pressurized Water Reactors and Fast Neutron Reactors*, Lavoisier Publishing, Paris, France, 1999). The frictionless model is used for the mechanical contact between the fuel and the clad. More input parameters for this problem are listed in **Table 2**.

A 2D axisymmetric (R-Z) model is used for this problem, as shown in **Fig. 3**. The pellet has 10 radial elements in the model. In BISON and CAMPUS, the pellet has 22 radial elements (Williamson et al., 2012) and 15 radial elements (Liu et al., 2016). The material models used in NECP-CALF, BISON, and CAMPUS are listed in **Table 3**.

Fig. 4 shows the pellet centerline temperature varying with the burnup. According to this figure, it can be seen that all the temperature evolutions can be divided into 6 stages:

Table 2
Input parameters for the UO₂-Zr fuel rod simulation.

| | |
|--|----------------------|
| Linear average power (W/cm) | 200 |
| Fast neutron flux ($\text{n/m}^2 \text{s}$) | 9.5×10^{17} |
| Coolant pressure (MPa) | 15.5 |
| Coolant temperature (K) | 530 |
| Coolant convection coefficient ($\text{W/m}^2 \text{K}$) | 7500 |
| Rod fill gas | Helium |
| Fill gas initial pressure (MPa) | 2.0 |
| Initial fuel density | 95% theoretical |
| Fuel densification | 1% theoretical |
| Burnup at full densification (MWd/kgU) | 5 |

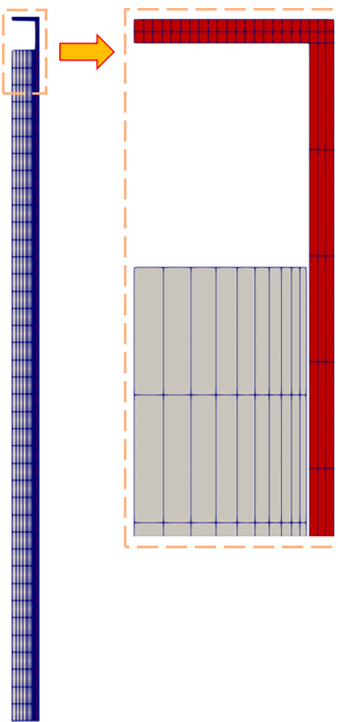


Fig. 3. Geometry and mesh of the $\text{UO}_2\text{-Zr}$ fuel rodlet.

Table 3
Material models used in NECP-CALF, BISON (Williamson et al., 2012) and CAMPUS (Liu et al., 2016).

| Material models | NECP-CALF | BISON | CAMPUS |
|---|---------------------|---------------------|-------------------|
| UO_2 thermal conductivity | Fink-Lucuta | Fink-Lucuta | Fink-Lucuta |
| UO_2 densification | ESCORE | ESCORE | ESCORE |
| UO_2 swelling | MATPRO | MATPRO | MATPRO |
| UO_2 cracking | smeared cracking | smeared cracking | \ |
| UO_2 creep | MATPRO | MATPRO | MATPRO |
| Intragranular fission gas diffusion solve | PolyPole-1 | FORMAS | FAST |
| Intergranular fission gas saturation | White and Tucker | White and Tucker | White and Tucker |
| Zr-4 thermal creep | Hayes and Kassner | Hayes and Kassner | Hayes and Kassner |
| Zr-4 irradiation creep | Hoppe | Hoppe | Hoppe |

- (1) In the beginning, the pellet centerline temperature rises from 530 K to about 1275 K over 3 h because of the first rise to power (it corresponds to the vertical line at 0 MWd/kgU for the burnup accumulated in the first rise to power is negligible).
- (2) After the first rise to power, the fuel densification increases the gap width at the early stage of the depletion (0–2 MWd/kgU), which results in the slight rising of the temperature.
- (3) With the burnup increasing, the swelling of the fuel and the cladding creep reduces the gap width, causing the pellet centerline temperature to decrease during 2–22 MWd/kgU in NECP-CALF and BISON or 2–10 MWd/kgU in CAMPUS.
- (4) After the fission gas begins to be released to the gap, the gap heat transfer is aggravated by the lower thermal conductivity of the gas mixtures, causing the pellet centerline temperature to rise again during 22–28 MWd/kgU in NECP-CALF and BISON or 10–22 MWd/kgU in CAMPUS.
- (5) With the burnup increasing, the swelling of the fuel and the creep of the cladding offset the aggravation of the gap heat transfer caused by the released fission gas, resulting in the decreasing of

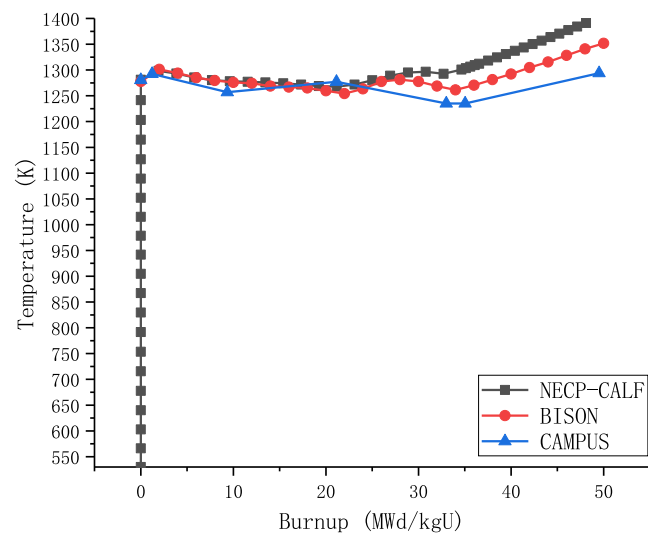


Fig. 4. Pellet centerline temperature versus burnup.

the temperature during 28–33 MWd/kgU in NECP-CALF and BISON or 22–33 MWd/kgU in CAMPUS.

- (6) After the gap closure, the pellet centerline temperature keeps rising due to the decreasing thermal conductivity of the fuel during 33–50 MWd/kgU.

It can also be seen that the results from NECP-CALF are in good agreement with those from BISON at the early stage of depletion. When the burnup is higher, the temperature from NECP-CALF is getting higher than it from BISON and the max difference between them is about 50 K. The difference may be caused by the different fission gas release, which will be presented later. The max difference between NECP-CALF and CAMPUS is relatively larger, which is about 100 K. It may attribute to the different models adopted in these two codes, such as the different mechanical parameters, thermal expansion coefficients and fission gas behavior models.

Fig. 5 shows the fission gas release fraction varying versus burnup. The activation burnup of the fission gas release from NECP-CALF is found to be in good agreement with it from BISON, which is about 22 MWd/kgU. However, when the burnup is higher, the fission gas release from NECP-CALF is getting larger than that of BISON, which might attribute to the different algorithms to solve the fission gas

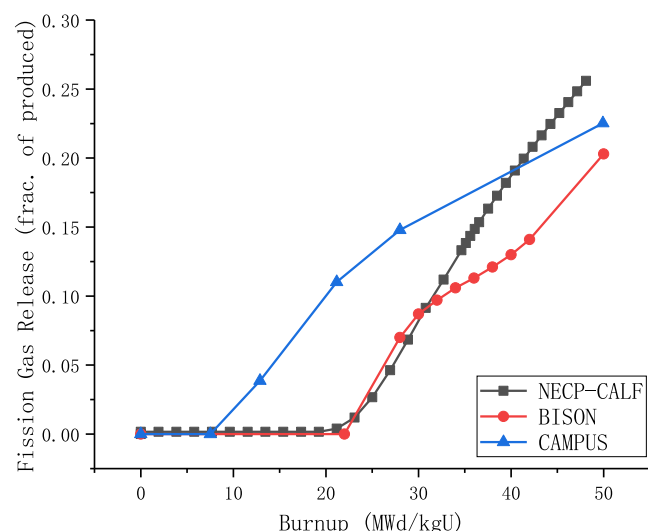


Fig. 5. Fission gas release versus burnup.

diffusion equation and the different parameters in the model. Compared with NECP-CALF and BISON, the activation burnup of the fission gas release from CAMPUS is lower, which might attribute to the different fission gas behavior models. Considering that the fission gas release computation model still exists much uncertainty (Pastore et al., 2015); the differences between these three codes are acceptable.

Fig. 6 shows the plenum pressure varying versus burnup. It can be seen that the plenum pressure evolutions can be divided into 3 stages:

- (1) In the beginning, the plenum pressure rises over 3 h because of the first rise to power.
- (2) After the first rise to power, the plenum pressure remains stable until the fission gas begins to be released.
- (3) After the fission gas begins to be released, the plenum pressure rises again.

Due to the early release of the fission gas mentioned above, the second stage of CAMPUS is very short.

The gap width varying with the burnup is shown in Fig. 7. The thermal expansion causes a sudden reduction of the gap width during the first rise to power. Then the gap width rises slightly due to the fuel densification. With the burnup increasing, the swelling of the fuel and the creep of the cladding make the gap width decrease linearly. The gap closure occurs at about 35 MWd/kgU. It can be seen that the results from these three codes are very close at high burnup. However, CAMPUS predicts a significantly larger gap width at low burnup. It may attribute to the smeared cracking model. The smeared cracking model will increase the pellet diameter and decrease the gap width, but the smeared cracking model is not adopted in CAMPUS.

It can be concluded that the differences between the results from these three codes are acceptable, which demonstrates the fuel behavior capabilities of NECP-CALF.

5. Mixed dimensional approach verification

In this section, a small-scale UO₂-Zr fuel rod with azimuthally asymmetric cladding temperature is designed and simulated using three approaches: the mixed dimensional approach (referred to as MDA), the 3D approach, and an approach in which all of the axial layers are 2D (referred to as 2.5D). The results are compared to verify the mixed dimensional approach. To save the time cost and improve the convergence, the simulations only consider the heat conduction, gap heat transfer, elasticity and thermal expansion. The material models are also

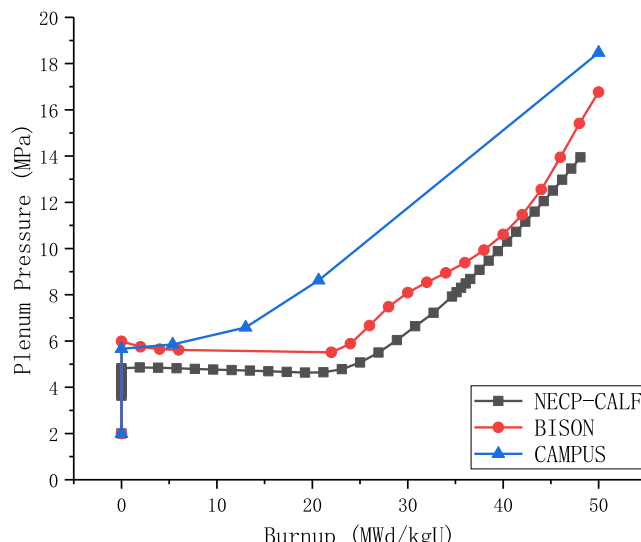


Fig. 6. Plenum pressure versus burnup.

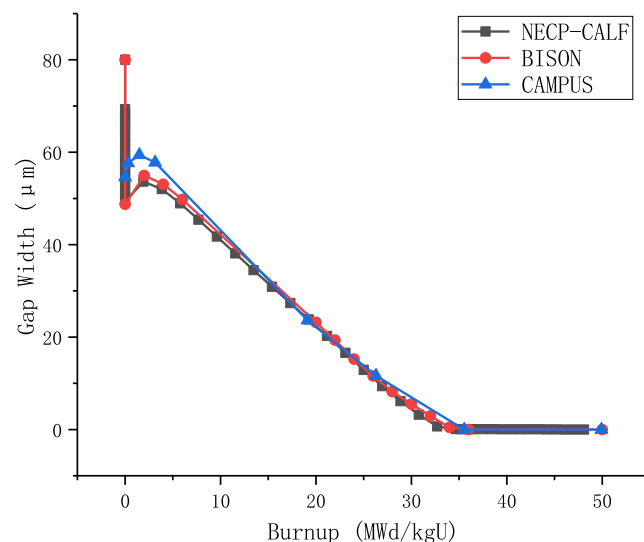


Fig. 7. Gap width versus burnup.

simplified as constants. It is reasonable for the verification because the approximation of the mixed dimensional approach is independent on the material models.

The geometry parameters and material parameters of the fuel rod are listed in Table 4. The coolant pressure of the fuel rod is 15 MPa. The axial distribution of the linear heat rate is shown in Fig. 8, in which the “axial position” means the distance from the bottom of the fuel pellet stack to the given point. From the axial position of 5 cm to the axial position of 10 cm, the cladding temperature is set to be azimuthally asymmetric. The distribution of the cladding temperature in this region is

$$T(\theta, z) = 615 + 25 \times (\cos\theta + 1) \times (\cos(72 \times (z - 7.5)) + 1) \quad (46)$$

where T is the cladding temperature (K), θ is the azimuthal angle in the vertical view of the fuel rod (°), z is the distance from the bottom to the given point (cm). At the middle of the fuel rod, the azimuthal distribution of the cladding temperature is shown in Fig. 9. For the other regions of the fuel rod, the cladding temperature is set to be uniform with the value of 615 K.

In MDA, the axial layer division is shown in Fig. 10. All the axial layers have the same length. Since the fuel rod is symmetric with respect to the X axis, as shown in Fig. 9, only half of the fuel rod is modelled. The 2D model and 1D model used in MDA is shown in Fig. 11. The model used in the full 3D simulation is shown in Fig. 12, in which the number of the axial elements is the same as the number of the layers in MDA. As for the 2.5D approach, the only difference between it and MDA is that it uses the 2D model for all the layers. Since the finite strain method is used in

Table 4

Geometry parameters and material parameters of the small-scale UO₂-Zr fuel rod.

| | |
|--|----------------------|
| Length of fuel pellet stack (cm) | 15.0 |
| Length of upper plenum (cm) | 1.0 |
| Fuel pellet diameter (cm) | 0.69 |
| Cladding inner diameter (cm) | 0.7 |
| Cladding outer diameter (cm) | 0.8 |
| Thermal conductivity of fuel (Wm ⁻¹ K ⁻¹) | 3.0 |
| Thermal conductivity of cladding (Wm ⁻¹ K ⁻¹) | 16.0 |
| Young's modulus of fuel (GPa) | 219.0 |
| Poisson's ratio of fuel | 0.345 |
| Young's modulus of cladding (GPa) | 75.0 |
| Poisson's ratio of cladding | 0.3 |
| Thermal expansion coefficient of fuel (K ⁻¹) | 1.0×10^{-5} |
| Thermal expansion coefficient of cladding (K ⁻¹) | 5.0×10^{-6} |
| Rod fill gas | Helium |
| Fill gas initial pressure (MPa) | 2.0 |

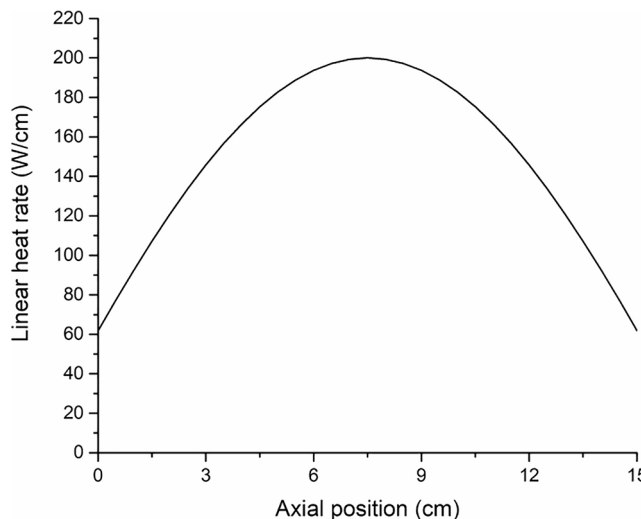


Fig. 8. Axial distribution of the linear heat rate of the small-scale UO₂-Zr fuel rod.

the mechanical computation, a 20-hour transient process with the time interval of 1 h is used to raise the power, temperature and pressure from the initial values to the steady-state values.

The results are compared to verify MDA. The axial distributions of the pellet max temperatures are shown in Fig. 13(a). It can be seen that the pellet max temperatures from the three simulations are in good agreement. The temperatures from the 3D simulation are slightly lower than the temperatures from the other two simulations at the middle axial position of the fuel rod because the heat conduction along the axial direction decreases the temperatures. Fig. 13(b) shows the differences in the pellet max temperatures comparing the MDA and 2.5D simulation respectively to the 3D simulation along the axial direction. In the non-axisymmetric region, the differences of the two simulations are almost the same. In the axisymmetric regions, the difference of the MDA simulation is greater than the difference of the 2.5D simulation. The possible reason is that the 2D and 3D model have the same radial mesh density but the radial mesh density of the 1D model is different from the 2D and 3D model, which can be seen in Figs. 11 and 12. Since the purpose of the MDA is to improve the efficiency while keeping the same accuracy level with the 3D simulation, the results from the MDA are compared to those from the 3D simulation. The comparison shows that the difference between the MDA simulation and the 3D simulation is less than 10 K, demonstrating the good accuracy of MDA for the

temperature.

The axial distributions of the cladding max Mises stresses are shown in Fig. 14(a). In the axisymmetric regions, the MDA simulation, in which the 1D model is used, predicts higher stresses, and the 2.5D simulation predicts lower stresses compared to the 3D simulation. In the non-axisymmetric region, both the MDA simulation and the 2.5D simulation predict higher stresses. However, all the discrepancies are very small compared to the absolute value of stress (about 80 MPa). It should be noted that there are discontinuous points at the junctures of the axisymmetric region and the non-axisymmetric region for the cladding stresses. Fig. 14(b) shows the difference in the max cladding Mises stresses comparing the MDA and 2.5D simulation respectively to the 3D simulation along the axial direction. It can be seen that the max difference between the MDA and the 3D simulation is lower than 2.5 MPa, demonstrating the good accuracy of MDA for the cladding Mises stress.

It should be mentioned that the 3D analysis might not be more accurate than the 1D solution for the 1D axisymmetric problems, especially when the mesh is not finer enough. Here the 3D simulation is taken as the reference not the “true” solution.

The memory costs of the three simulations are listed in Table 5. It can be seen that the 3D simulation costs the least memory and the 2.5D simulation costs the largest memory. The memory of the MDA simulation is slightly larger than the memory of the 3D simulation. It attributes to the extra memory cost by the MultiApp function used in the MDA simulation and the 2.5D simulation. Table 6 shows the time costs for the three simulations. MDA saves 87.5% of the 3D time cost and 62.7% of the 2.5D time cost, demonstrating obviously higher efficiency of MDA.

It can be concluded that the MDA and 2.5D simulations can model the non-axisymmetric fuel element with reasonable accuracy and better efficiency than the 3D simulations.

6. SCWR-FQT flow blockage simulation

As one of the SCWR R&D activities ongoing worldwide, the supercritical water reactor fuel qualification test (SCWR-FQT) project (Ruzickova et al., 2015) designed a small-scale fuel bundle to carry out the fuel tests under the supercritical-water-cooled conditions in a research reactor. The SCWR-FQT fuel bundle contains 4 fuel rods with a pressure tube to maintain the supercritical water conditions. Wire wrap spacer is adopted in the SCWR-FQT fuel bundle to enhance the coolant mixing flow between sub-channels and keep the cooling channels by preventing the fuel rod from contacting adjacent rods. However, the wire wrap utilization may bring some severe problems, e.g., the detachment of the wire wrap, causing local flow path blockage inside the test section (Liu et al., 2013). When the flow blockage occurs in a certain

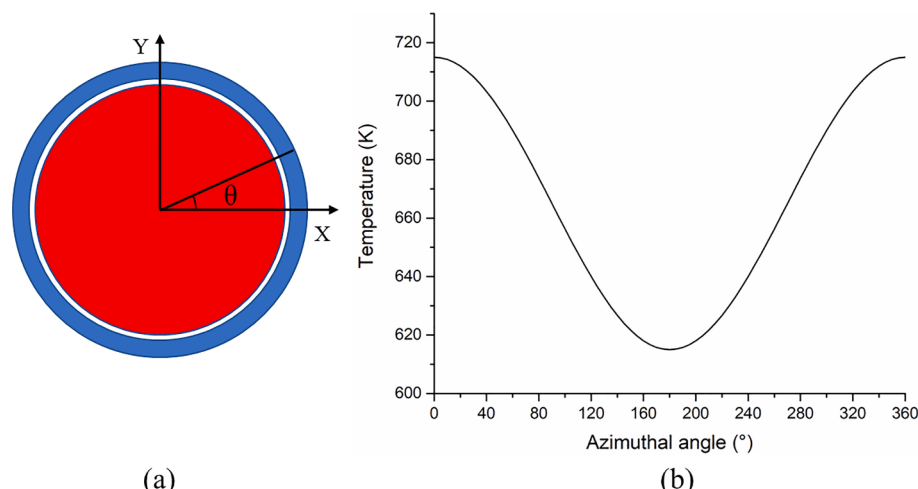


Fig. 9. (a) vertical view of the small-scale UO₂-Zr fuel rod and (b) azimuthal distribution of the cladding temperature at the middle of the fuel rod.

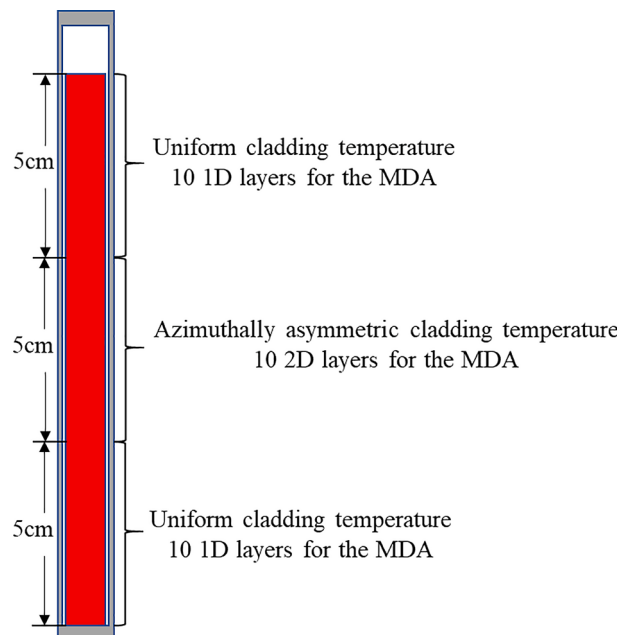


Fig. 10. Axial layer division of the small-scale UO₂-Zr fuel rod in the MDA.

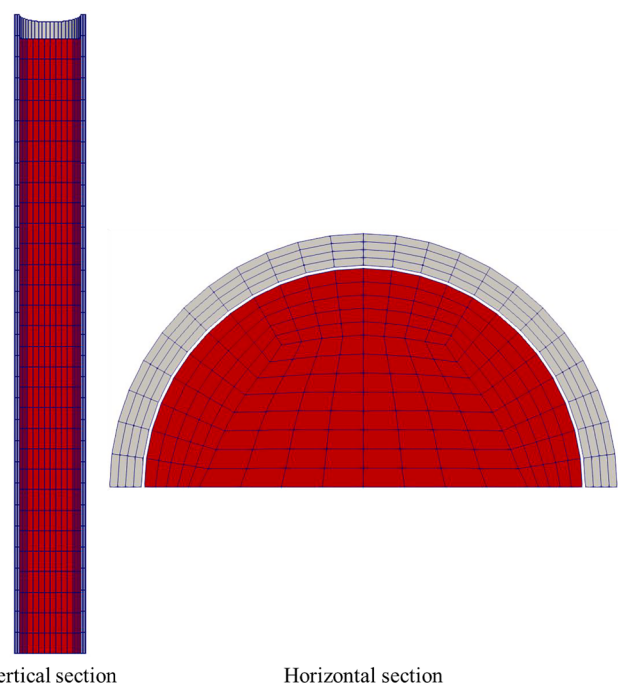


Fig. 12. the 3D model of the small-scale UO₂-Zr fuel rod.

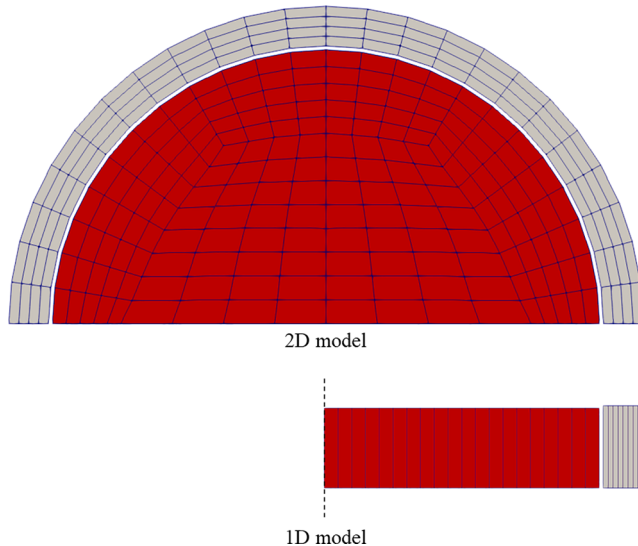


Fig. 11. the 2D model and the 1D model of the small-scale UO₂-Zr fuel rod used in the MDA.

sub-channel, the coolant flux will be lowered at the blockage position and. Then the cladding temperature at that position will rise significantly, causing a non-axisymmetric cladding temperature condition.

The SCWR-FQT fuel rod is simulated using NECP-CALF to study the impact of the flow blockage on the fuel rod performance. The designed parameters and conditions are from reference (Ruzickova et al., 2015; Liu et al., 2013; Vojacek et al., 2015) and (Maráczky et al., 2015). Fig. 15 shows the cross-section of the SCWR-FQT fuel bundle, and Fig. 16 shows the vertical section of the SCWR-FQT fuel rod. The radius of the UO₂ fuel pellet is 3.45 mm. The initial gap width is 50 μm, and the plenum gas is He with the initial pressure of 7 MPa. The thickness of the stainless steel 316 cladding is 0.5 mm. The fuel stack consists of approximately 87 pellets with a height of 600 mm. The height of the upper plenum is 40 mm.

The coolant pressure of the SCWR-FQT fuel bundle is 25 MPa. The power history is assumed to be divided into 2 periods: in the beginning,

the power rises from zero to the steady-state power linearly over 3 h; then, the power is held constant for 6 months, as shown in Fig. 17. The steady-state power of a fuel rod is 15.75 kW. The axial power distribution is shown in Fig. 18. Fig. 19 shows the flow blockage caused by the wire wrap detachment in the SCWR-FQT fuel bundle. It can be seen that the blockage reduces the flow area, which lowers the coolant flux and then increases the cladding temperature at the sub-channel. In this work, Rod 1 with flow blockage at SC2, SC4, and SC5 is simulated. The wire wrap detachment is assumed to occur immediately after the first rise to power at the height of 0.2 m, causing the cladding temperature to rise in 1 s, called “cladding temperature jump” in this paper shown in Fig. 20. The axial distribution of the sub-channel cladding temperature after the wire wrap detachment is shown in Fig. 21, which is the boundary condition in the simulation.

The mixed dimensional approach is used to model the fuel rod. The layer division of the fuel rod is shown in Fig. 22, depending on the variance of the power and the cladding temperature along the axial direction. There are 43 layers in all. At the region lower than 0.35 m, the difference between the cladding temperature in the blocked sub-channel and the cladding temperature in the normal sub-channel is significant. it is meshed into 37 layers and the 2D model is used for every layer. From 3.5 m to 0.6 m in the axial direction, the difference is negligible, and it is divided into 6 layers, and the 1D model is used. The 2D model is shown in Fig. 23 and the 1D model is shown in Fig. 24.

It should be noted that the normal sub-channels are assumed to have the same cladding temperature, which makes the fuel rod symmetric. Taking the fuel rod with the blocked SC2 as an example, as shown in Fig. 23(a), the fuel rod is symmetric with respect to the dot-and-dash line. So only half of the fuel rod is modeled in the 2D model.

In this simulation, the 1D model is actually a set of elements with one mesh along the axial direction. The mechanical boundary conditions of it are shown in Fig. 24. The axial pellet pressure can be computed as

$$P_{\text{pellet_axial}} = P_{\text{gas}} + \rho_{\text{pellet}} g(H - Z)$$

where $P_{\text{pellet_axial}}$ is the axial pellet pressure (Pa), P_{gas} is the plenum gas pressure (Pa), ρ_{pellet} is the density of the pellet (kg/m³), g is the gravitational acceleration (9.8 m/s²), H is the height of the fuel rod (m), Z is the distance from the bottom to the axial layer (m). The clad axial

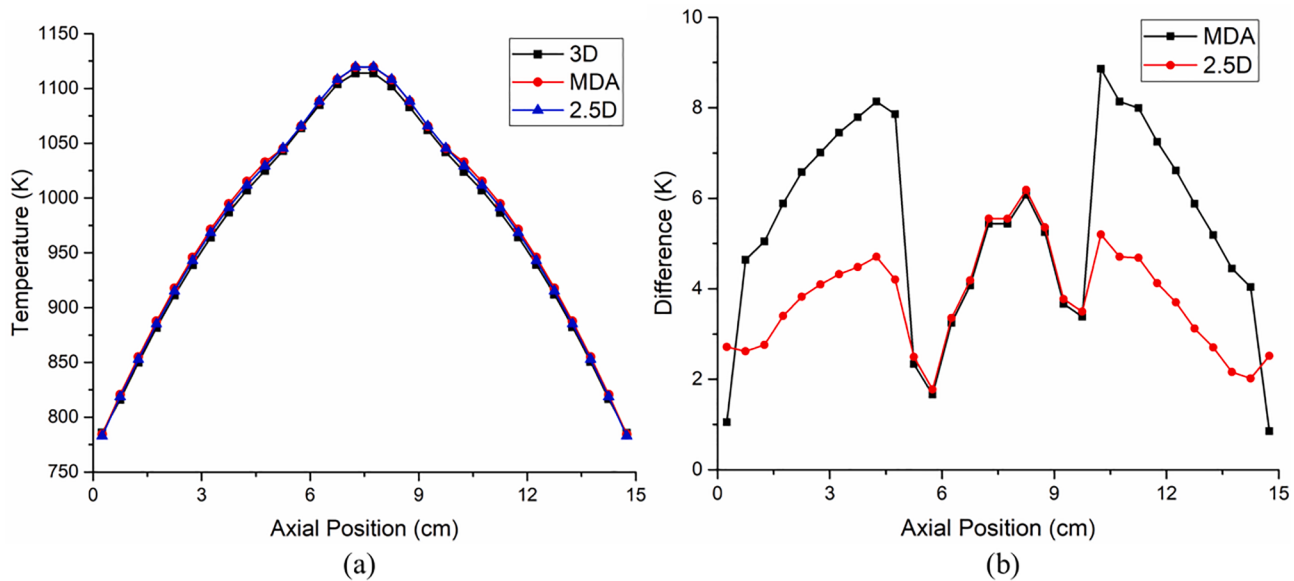


Fig. 13. (a) Pellet max temperatures along the axial direction. (b) Difference in the pellet max temperatures compared with the 3D simulation along the axial direction.

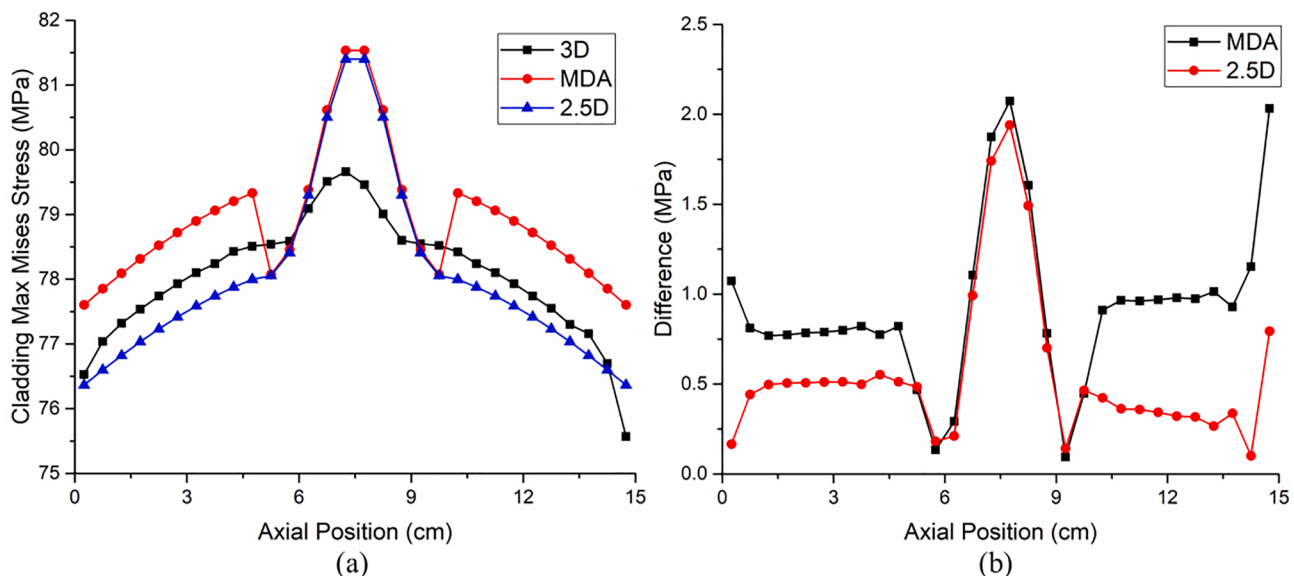


Fig. 14. (a) Cladding max Mises stresses along the axial direction. (b) Difference in the cladding max Mises stresses compared with the 3D simulation along the axial direction.

Table 5

Memory costs of the small-scale UO₂-Zr fuel rod simulations.

| Geometrical Model | MDA | 2.5D | 3D |
|-------------------|-------|-------|-------|
| Memory/MB | 310.0 | 474.6 | 291.3 |

Table 6

Time costs of the small-scale UO₂-Zr fuel rod simulations.

| Geometrical Model | MDA | 2.5D | 3D |
|-------------------|-----|------|-----|
| Time/minutes | 38 | 102 | 304 |

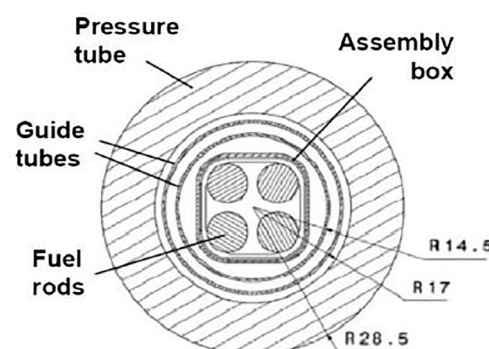


Fig. 15. Cross-section of the SCWR-FQT fuel bundle (Ruzickova et al., 2015).

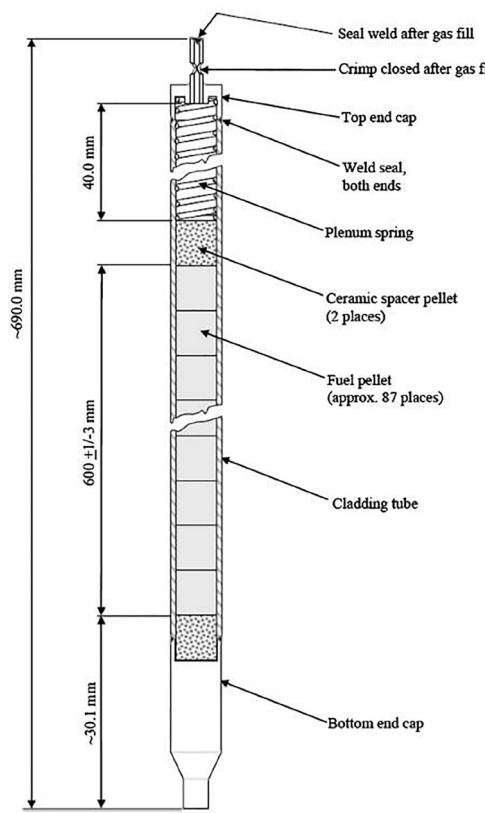


Fig. 16. Vertical section of the SCWR-FQT fuel rod (Vojacek et al., 2015).

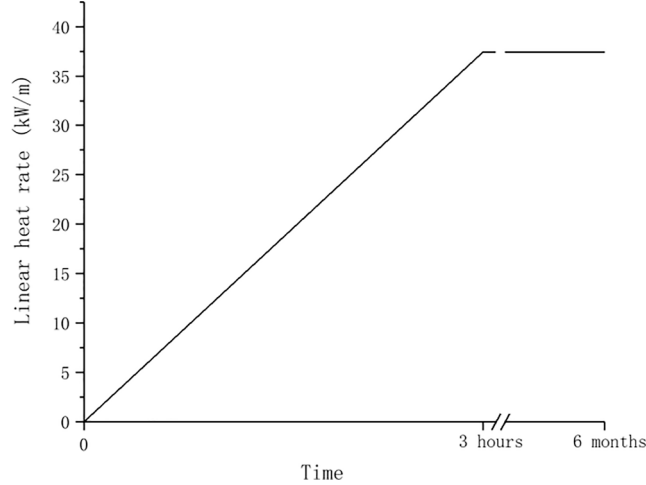


Fig. 17. Linear heat rate history at the height of 0.2 m with flow blockage at SC2.

pressure can be computed as

$$P_{\text{clad_axial}} = P_{\text{coolant}} \frac{r_o^2}{r_o^2 - r_i^2} - P_{\text{gas}} \frac{r_i^2}{r_o^2 - r_i^2} + \rho_{\text{clad}} g (H - Z)$$

where $P_{\text{clad_axial}}$ is the clad axial pressure (Pa), P_{coolant} is the coolant pressure (Pa), r_o is the clad outer radius (m), r_i is the clad inner radius (m), P_{gas} is the plenum gas pressure (Pa), ρ_{clad} is the density of the clad (kg/m^3), g is the gravitational acceleration (9.8 m/s^2), H is the height of the fuel rod (m), Z is the distance from the bottom to the axial layer (m).

The 2D model uses the generalized plane strain method to handle the out of plane strains. The boundary conditions of the 2D model are shown

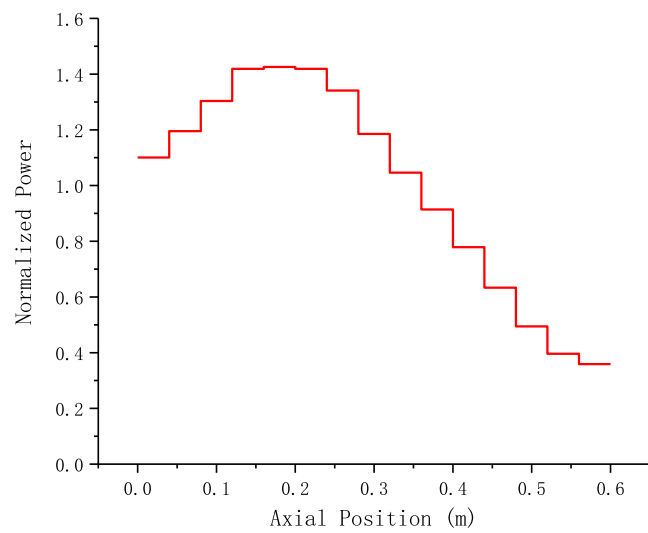


Fig. 18. Normalized axial power distribution (Liu et al., 2013).

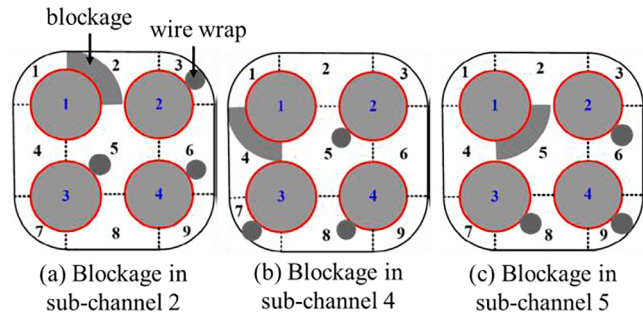


Fig. 19. Schematic illustration of the wire wrap blockage (Liu et al., 2013).

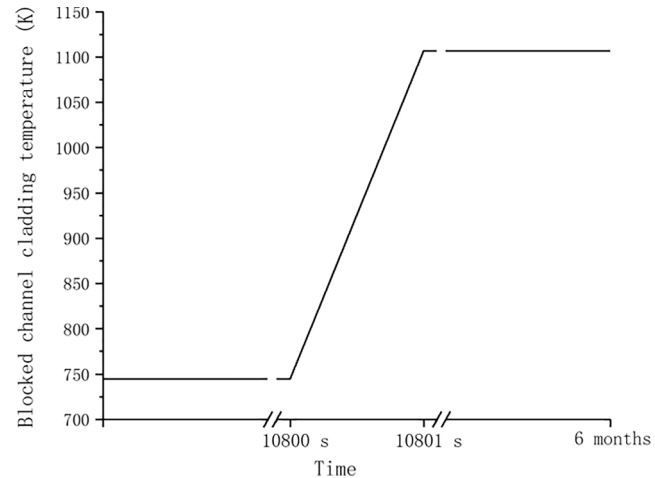


Fig. 20. Blocked channel cladding temperature history at the height of 0.2 m with flow blockage at SC2.

in Fig. 23(b). In the 2D model, the penalty boundary condition is applied to the symmetric surface of the clad on X displacement. It allows the clad to shift in the X direction while preventing a singularity in the mechanical computation. The out of plane pressures of the pellet and the clad are the same as those in the 1D model.

Fig. 25 shows the average plenum gas temperature varying with the time. It can be seen that the average plenum gas temperature rises rapidly by about 120 K during the first rise to power. After the power

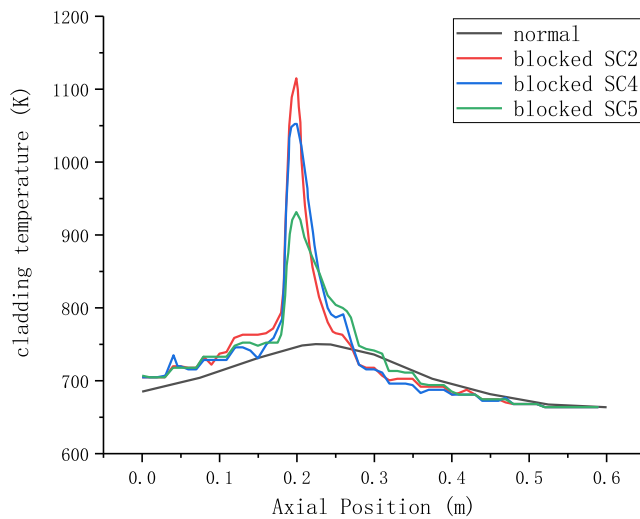


Fig. 21. Axial distribution of the sub-channel cladding temperature after the wire wrap detachment (Liu et al., 2013).

and the cladding temperature reach the steady-state, the temperature decreases gradually until the 40th day. Then the temperature remains stable until the end of the depletion. The difference in the temperature of the different flow blockage cases is found to be negligible. Compared with the cases with flow blockage, the temperature in the normal case is slightly lower. Fig. 26 shows the released fission gas moles varying with the time. It can be observed that the fission gas begins to be released at the same time in these four cases, but the released fission gas in the flow blockage cases is more than that in the normal case, which is caused by the higher fuel temperature in the flow blockage cases. The plenum pressure varying with the time is shown in Fig. 27. The evolution history of the plenum pressure is similar to the evolutionary history of the average plenum gas temperature at the early stage of the depletion. However, with the burnup increasing, the plenum pressure rises gradually rather than remains stable, which is caused by the fission gas release. The pressure from the flow blockage cases is 0.5 MPa higher than the normal case at the end of depletion. According to these results, the influence of the flow blockage on the global quantities is not very significant.

Compared to the global quantities, the differences in the local quantities of the flow blockage cases and the normal cases are more

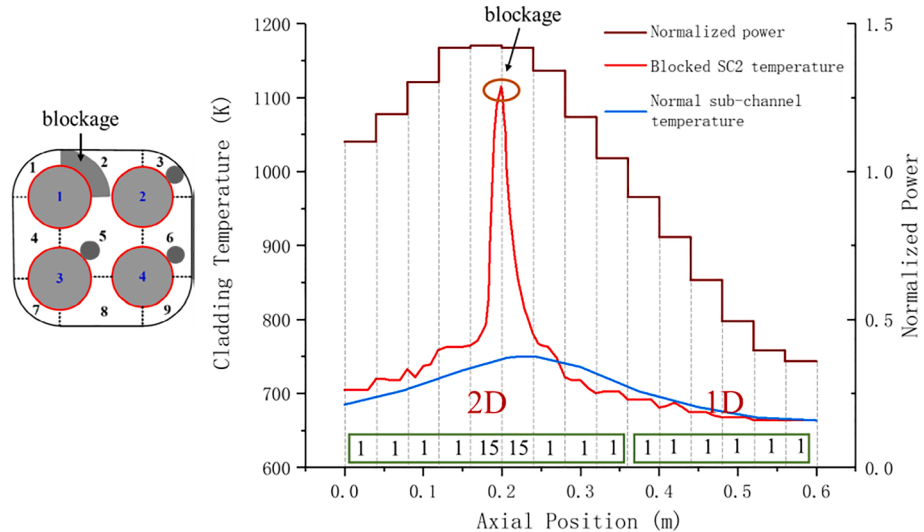


Fig. 22. Layer division of the SCWR-FQT fuel rod. The numbers in the green boxes mean the number of the layers between the dotted li. (For interpretation of the references to colour in this figure legend, the reader is referred to the web version of this article.)

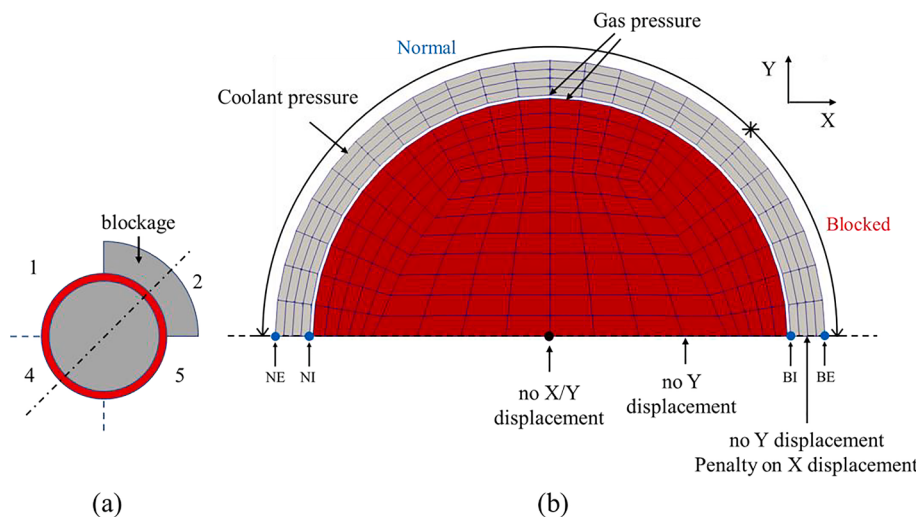


Fig. 23. (a) Symmetry of the fuel rod with the blocked SC2. (b) 2D model for the SCWR-FQT flow blockage simulation.

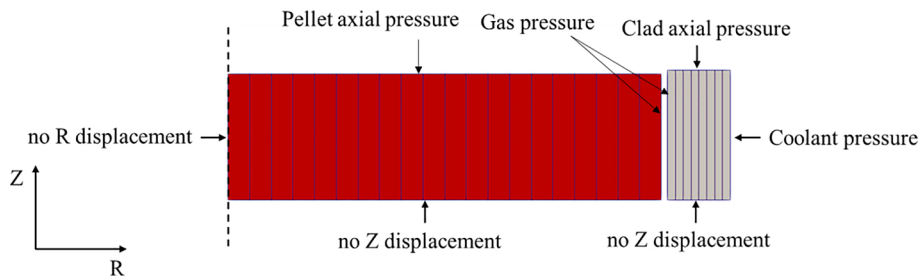


Fig. 24. 1D model for the SCWR-FQT flow blockage simulation.

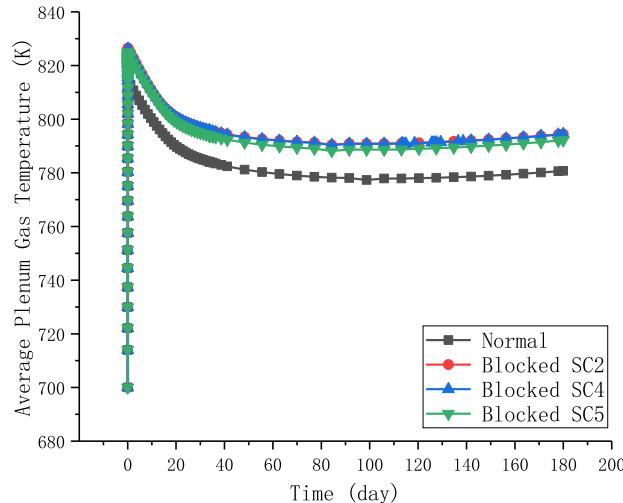


Fig. 25. Average plenum gas temperature versus time.

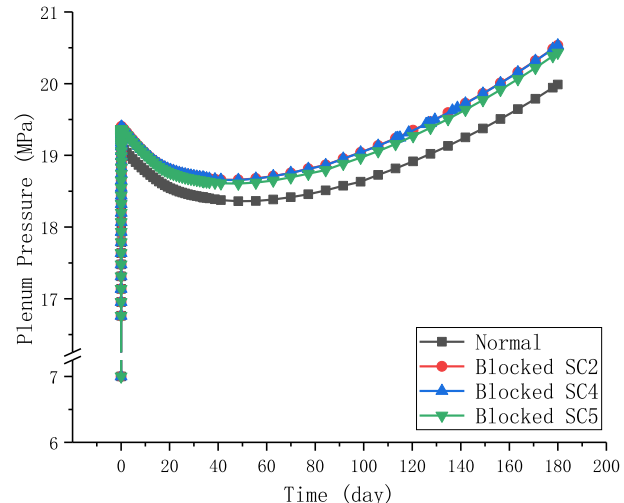


Fig. 27. Plenum pressure versus time.

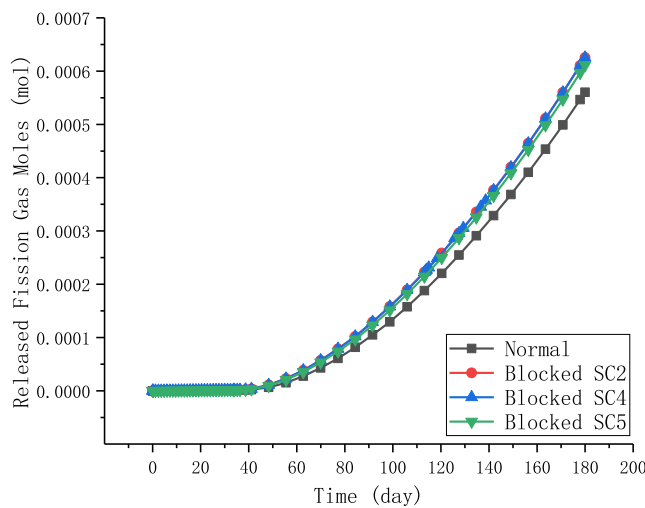


Fig. 26. Released fission gas moles versus time.

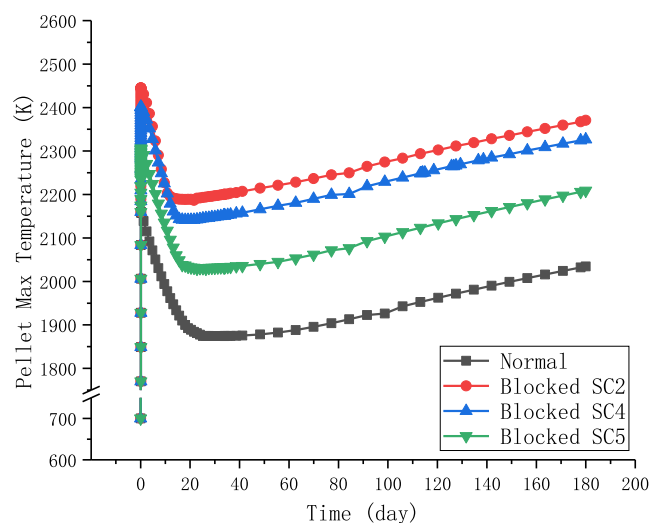


Fig. 28. Pellet max temperature versus time.

considerable. Fig. 28 shows the pellet max temperature varying versus time. It can be observed that the highest temperature occurs immediately after the first rise to power and the cladding temperature jump. Then the temperature decreases rapidly due to the reduction of the gap width. After the gap closure, the temperature rises gradually because of the lower thermal conductivity of the fuel. The case with the blocked SC2 is the severest, increasing the temperature by about 250 K compared with the normal case. Fig. 29 shows the axial distribution of the contact pressure at the final time step. The max contact pressures in these four cases are found to be the same, which is about 35 MPa. It should be

noted that there is a significant drop at the blockage position in the flow blockage cases. The reason of this drop is that the high cladding temperature at this position introduces the significant thermal creep, causing the cladding to deform more easily driven by the expansion of the pellet.

Fig. 30(a) and (b) respectively show the distribution of the temperature at the hottest layer from the case with the blocked SC2 before the cladding temperature jump (10800 s) and after the cladding temperature jump (10801 s). It can be seen that the higher cladding temperature at the blocked side causes the pellet max temperature point to move

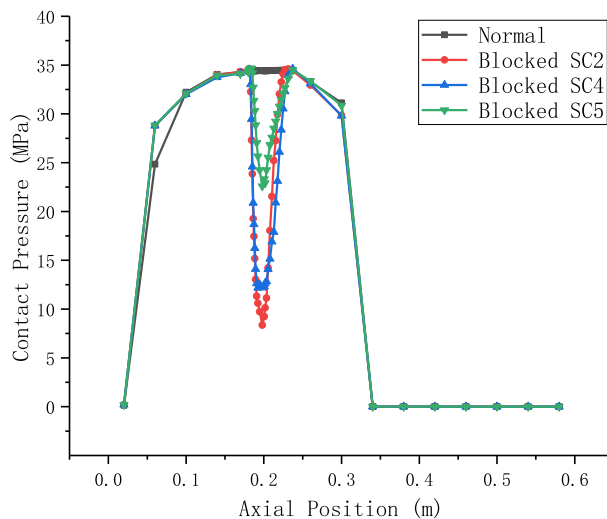


Fig. 29. Axial distribution of the contact pressure at the final time step.

slightly towards the blocked (right in the figures) side, resulting in the eccentric distributions. Fig. 31(a)–(c) show the distribution of the Mises stress of the cladding at the hottest layer from the case with the blocked SC2 and the time points are respectively before the cladding temperature jump (10800 s), when the stress exceeds the yield strength during the cladding temperature jump (10800.3 s) and after the cladding temperature jump (10801 s). It can be observed that the higher cladding temperature jump increases the Mises stresses significantly. The Mises stresses at the normal (left in the figures) side and at the blocked (right in the figures) side exceed the yield strength simultaneously. However, the Mises stress at the blocked side drops to a relatively low value very soon while the Mises stress at the normal side remains high. The reason is that the very high temperature at the blocked side induces significant creep deformation, which relaxes the stress at this position.

A series of time history plots of some quantities of interest at selected

locations from the hottest layer of the case with the blocked SC2 have been generated. Fig. 23(b) shows these locations, which are an exterior point at the normal side of the cladding (denoted as NE), an interior point at the normal side of the cladding (denoted as NI), an interior point at the blocked side of the cladding (denoted as BI), an exterior point at the blocked side of the cladding (denoted as BE), respectively. The results of the normal case at NE and NI are also presented and marked as E and I, respectively.

Fig. 32 shows the variance history of the Mises stress at the selected locations during the cladding temperature jump, and Fig. 33 shows the time history during the full depletion. NI, NE, BI, BE are from the SC2 flow blockage case and can be seen in Fig. 23(b); I and E mean the interior cladding point and the exterior cladding point from the normal case. It can be observed that the Mises stresses at the four points in the flow blockage case rise rapidly to the yield strength due to the significant temperature gradient during the cladding temperature jump. However, the extremely high temperature at the blocked side induces the large thermal creep at BI and BE and then causes the Mises stresses at these two locations to drop, which has also been shown in Fig. 31(c). The Mises stresses at the locations in the normal case remain stable and do not reach the yield strength in this period because there is no cladding temperature jump. After the cladding temperature jump, the Mises stresses at NI and NE decrease following the drop at the point BI and BE, as shown in Fig. 33. With the burnup increasing, the expanding pellet contacts the cladding and increases the Mises stresses at NI and NE to the yield strength again. The Mises stresses at the point BI and BE, however, retain a low value until the end of the depletion. It is caused by the stress relaxation due to the significant thermal creep.

Figs. 34–35 show the time histories of the effective creep strains, effective plastic strains and radial displacements at the selected locations during the full depletion respectively. It could be seen, the effective creep strains at BI and BE are far greater than those at other points, due to the higher temperature at the blocked side. The effective plastic strains at the locations in the flow blockage case are found to increase sharply during the cladding temperature jump but remain stable after that, which are significantly different from those in the normal case as

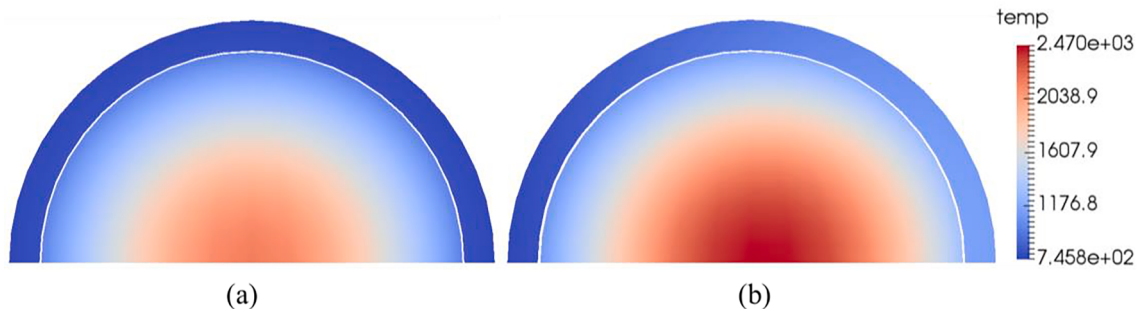


Fig. 30. Distribution of the temperature at the hottest layer from the case with the blocked SC2. (a) is before the cladding temperature jump (10800 s). (b) is after the temperature jump (10801 s).

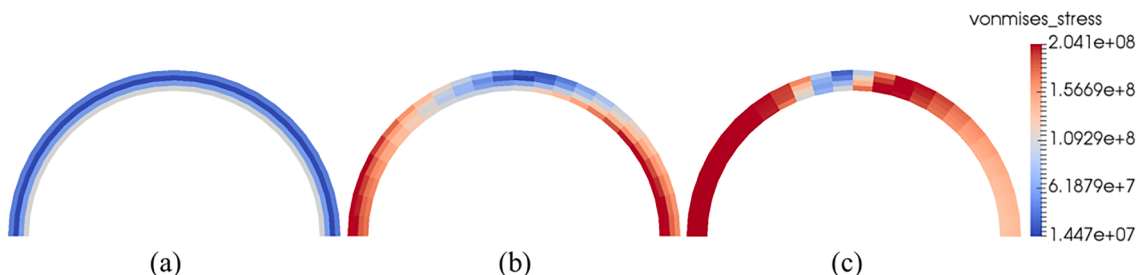


Fig. 31. Distribution of the Mises stress of the cladding at the hottest layer from the case with the blocked SC2. (a) is before the cladding temperature jump (10800 s). (b) is when the stress exceeds the yield strength during the cladding temperature jump (10800.3 s). (c) is after the cladding temperature jump (10801 s).

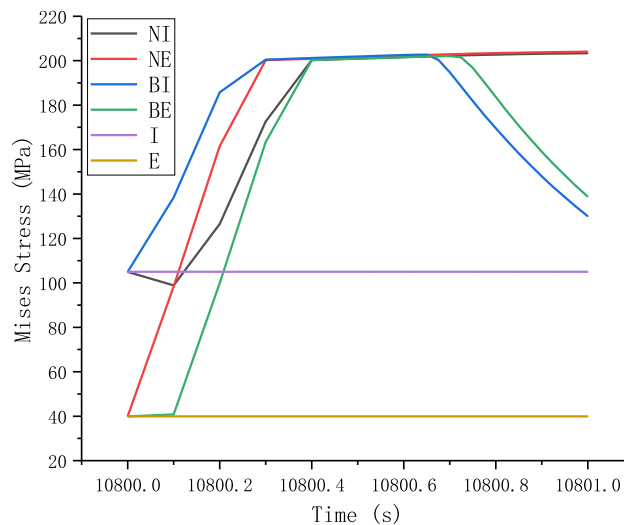


Fig. 32. Time history of the Mises stress at the selected locations during the cladding temperature jump.

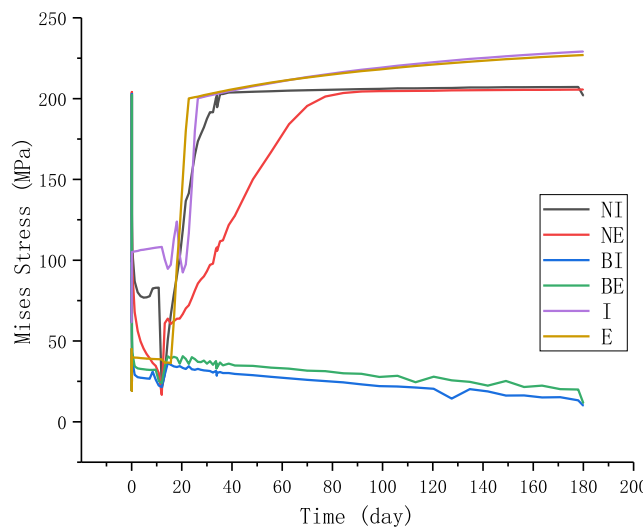


Fig. 33. Time history of the Mises stress at the selected locations during the full depletion.

shown in Fig. 35. The reason is that the cladding stresses are raised by the temperature gradient in the beginning and then are relaxed by the thermal creep. The radial displacements in the flow blockage case are greater than those in the normal case because of the more significant pellet expansion. It should be noted that the radial displacement at BI is more significant than that at BE, which means the cladding at the blocked side is getting thinner as the burnup increasing.

7. Summary

A multidimensional multiphysics fuel performance code named NECP-CALF is developed based on the MOOSE platform. The code includes fuel behavior models such as heat conduction, solid mechanics, gap heat transfer, swelling, densification, creep, fission gas release, etc. Besides the normal 1D, 2D and 3D models, a new geometrical approach called the mixed dimensional approach is developed in NECP-CALF. It is suitable for the fuel element, in which both the axisymmetric region and the non-axisymmetric region exist.

A traditional LWR UO₂-Zr fuel rod is simulated using NECP-CALF. Consistent results have been found by comparing NECP-CALF with

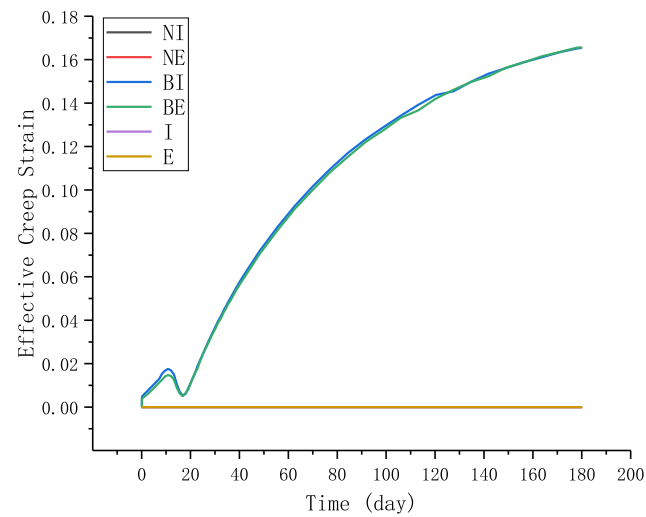


Fig. 34. Time history of the effective creep strain at the selected locations during the full depletion.

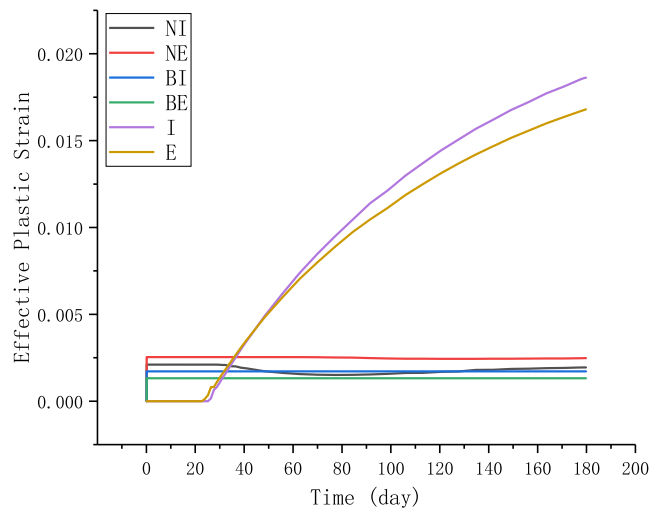


Fig. 35. Time history of the effective plastic strain at the selected locations during the full depletion.

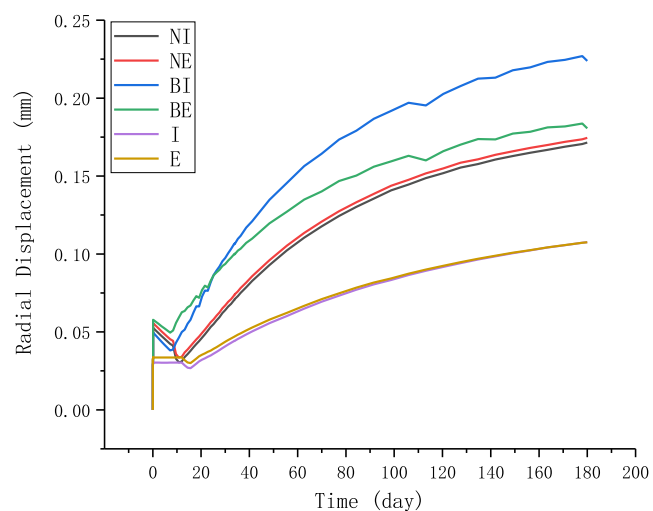


Fig. 36. Time history of the radial displacement at the selected locations during the full depletion.

BISON and CAMPUS. A small-scale UO₂-Zr fuel rod with azimuthally asymmetric cladding temperature is simulated to verify the mixed dimensional approach. Comparing the mixed dimensional approach and the full 3D simulation demonstrates that the mixed dimensional approach could improve efficiency while keeping the capability and accuracy to model the non-axisymmetric fuel element. The SCWR-FQT fuel rod with flow blockage is simulated to study the impact of the flow blockage accident on the fuel rod performance. The results indicate that the flow blockage would significantly increase the pellet max temperature and cause the plastic deformation of the cladding immediately after the cladding temperature jump, and this would cause the safety problems of the fuel rod.

Future works would include developing the fuel behavior models for more fuel types (such as plate fuels and ATF) and the coupling with high-fidelity neutronics and thermal-hydraulics codes.

CRediT authorship contribution statement

Zhouyu Liu: Conceptualization, Methodology, Writing - original draft. **Xiaobei Xu:** Software, Validation, Writing - review & editing. **Hongchun Wu:** Supervision, Visualization. **Liangzhi Cao:** Project administration, Data curation.

Declaration of Competing Interest

The authors declare that they have no known competing financial interests or personal relationships that could have appeared to influence the work reported in this paper.

Acknowledgements

The financial support from the National Science and Technology Major Project of China (2019ZX06002033) the Innovative Scientific Program of CNNC is highly appreciated.

References

- C.M. Allison, G.A. Berna, R. Chambers, E.W. Coryell, K.L. Davis, D.L. Hagman, D.T. Hagman, N.L. Hampton, J.K. Hohorst, R.E. Mason, M.L. McComas, K.A. McNeil, R.L. Miller, C.S. Olsen, G.A. Reymann, L.J. Siefken. SCDAP/RELAP5/MOD3.1 code manual, volume IV: MATPRO – a library of materials properties for light-water-reactor accident analysis. Technical Report NUREG/CR-6150, EGG-2720, Idaho National Engineering Laboratory, 1993.
- Altenbach H., Gorash Y. (2013) High-Temperature Inelastic Behavior of the Austenitic Steel AISI Type 316. In: Altenbach H., Kruch S. (eds) Advanced Materials Modelling for Structures. Advanced Structured Materials, vol 19. Springer, Berlin, Heidelberg. https://doi.org/10.1007/978-3-642-35167-9_3.
- H. Bailly, D. Ménessier, C. Prunier (Eds.), The Nuclear Fuel of Pressurized Water Reactors and Fast Neutron Reactors, Lavoisier Publishing, Paris, France, 1999.
- Berna, G A, Beyer, G A, Davis, K L, & Lanning, D D. FRAPCON-3: A computer code for the calculation of steady-state, thermal-mechanical behavior of oxide fuel rods for high burnup. United States. doi:10.2172/576110.
- Che, Y., Pastore, G., Hales, J., Shirvan, K., 2018. Modeling of cr 2o 3-doped uo 2 as a near-term accident tolerant fuel for lws using the bison code. Nucl. Eng. Des. 337, 271–278.
- Deng, Y., Shirvan, K., Wu, Y., Su, G., 2019. Utilization of 3d fuel modeling capability of bison to derive new insights in performance of advanced pwr fuel concepts. J. Nucl. Mater. 516, 271–288.
- Desu, R.K., Nitin Krishnamurthy, H., Balu, A., Gupta, A.K., Singh, S.K., 2016. Mechanical properties of austenitic stainless steel 304l and 316l at elevated temperatures. J. Mater. Res. Technol. 5 (1), 13–20.
- Elton, P.T., Lassmann, K., 1987. Calculational methods for diffusional gas release. Nucl. Eng. Des. 101 (3), 259–265.
- Fink, J.K., Chasanov, M.G., Leibowitz, L., 1981. Thermophysical properties of uranium dioxide. J. Nucl. Mater. 102 (1–2), 17–25.
- Forsberg, K., Massih, A.R., 1985a. Diffusion theory of fission gas migration in irradiated nuclear fuel uo₂. J. Nucl. Mater. 135 (2–3), 140–148.
- Forsberg, K., Massih, A.R., 1985b. Fission gas release under time-varying conditions. J. Nucl. Mater. 127 (2–3), 141–145.
- Gaston, Derek R., et al., 2015. Physics-based multiscale coupling for full core nuclear reactor simulation. Ann. Nucl. Energy 84, 45–54.
- Gaston, D., Newman, C., Hansen, G., Lebrun-Grandjean, D., 2009. Moose: a parallel computational framework for coupled systems of nonlinear equations. Nucl. Eng. Des. 239 (10), 1768–1778.
- Hales, J. D., Williamson, R. L., Novascone, S. R., Pastore, G., Spencer, B. W., Stafford, D. S., Gamble, K. A., Perez, D. M., & Liu, W. BISON Theory Manual The Equations behind Nuclear Fuel Analysis. United States. doi:10.2172/1374503.
- Hales, J.D., Williamson, R.L., Novascone, S.R., et al., 2013. Multidimensional multiphysics simulation of TRISO particle fuel. J. Nucl. Mater. 443 (1–3), 531–543.
- Hayes, T.A., Kassner, M.E., 2006. Creep of zirconium and zirconium alloys. Metall. Mat. Trans. A 37, 2389–2396. <https://doi.org/10.1007/BF02586213>.
- Hermannson, P., Massih, A.R., 2002. An effective method for calculation of diffusive flow in spherical grains. J. Nucl. Mater. 304 (2), 204–211.
- N.E. Hoppe, Engineering model for zircaloy creep and growth, in: Proceedings of the ANS-ENS International Topical Meeting on LWR Fuel Performance, Avignon, France, April 21–24, 1991, pp. 157–172.
- Jackson, P.A., Turnbull, J.A., White, R.J., 1990. Enigma fuel performance code. Nucl. Energy 29 (2), 107–114.
- Knoll, D.A., Chacon, L., Margolin, L.G., Mousseau, V.A., 2003. On balanced approximations for time integration of multiple time scale systems. J. Comput. Phys. 185 (2), 583–611.
- Knoll, D.A., Keyes, D.E., 2004. Jacobian-free newton-krylov methods: a survey of approaches and applications. J. Comput. Phys. 193 (2), 357–397.
- Lanning, D D, & Hann, C R. Review of methods applicable to the calculation of gap conductance in Zircaloy-clad UO₂ fuel rods. United States. doi:10.2172/4209005.
- Lassmann, K., 1992. Transuranus: a fuel rod analysis code ready for use. J. Nucl. Mater. 188 (C), 295–302.
- Lassmann, K., Benk, H., 2000. Numerical algorithms for intragranular fission gas release. J. Nucl. Mater. 280 (2), 127–135.
- Liu, X. J., Yang, T. , & Cheng, X. (2013). Thermal-hydraulic analysis of flow blockage in a supercritical water-cooled fuel bundle with sub-channel code. Annals of nuclear energy, 59(sep.), 194–203.
- Liu, R., Cai, J., & Zhou, W. (2020). Multiphysics modeling of thorium-based fuel performance with a two-layer sic cladding in a light water reactor. Annals of nuclear energy, 136(Feb.), 107036.1–107036.12.
- Liu, R., Prudil, A., Zhou, W., Chan, P.K., 2016. Multiphysics coupled modeling of light water reactor fuel performance. Prog. Nucl. Energy 91, 38–48.
- Lucuta, P.G., Matzke, H.J., Hastings, I.J., 1996. A pragmatic approach to modelling thermal conductivity of irradiated UO₂ fuel: Review and recommendations. J. Nucl. Mater. 232 (2–3), 166–180.
- Luscher, Walter G, & Geelhood, Kenneth J. Material Property Correlations: Comparisons between FRAPCON-3.4, FRAPTRAN 1.4, and MATPRO. United States. doi:10.2172/1030897.
- Maráczky, C., Hegyi, G., Trosztel, I., and Temesvári, E. (December 9, 2015). “Control Rod Withdrawal Analysis of the Supercritical Water Reactor-Fuel Qualification Test Facility in the LVR-15 Research Reactor.” ASME. ASME J of Nuclear Rad Sci. January 2016; 2(1): 011004. <https://doi.org/10.1115/1.4030933>.
- Maráczky, C., Hegyi, G., Trosztel, I., Temesvári, E., 2015. Control rod withdrawal analysis of the supercritical water reactor-fuel qualification test facility in the LVR-15 research reactor. ASME J Nucl. Rad. Sci. 2 (1), 011004. <https://doi.org/10.1115/1.4030933>.
- Martineau, R., et al., 2020. Multiphysics for nuclear energy applications using a cohesive computational framework. Nucl. Eng. Des. 367.
- Kenneth C. Mills. Recommended Values of Thermophysical Properties for Selected Commercial Alloys. Woodhead Publishing, 2002.
- Mousseau, V.A., Knoll, D.A., 2006. Temporal accuracy of the nonequilibrium radiation diffusion equations applied to two-dimensional multimaterial simulations. Nucl. Sci. Eng. 154 (2), 174–189.
- Nakajima, T., Saito, H., Osaka, T., 1994. Femaxi-iv: a computer code for the analysis of thermal and mechanical behavior of light water reactor fuel rods. Nucl. Eng. Des. 148 (1), 41–52.
- Olander, D. R. Fundamental aspects of nuclear reactor fuel elements. United States. doi: 10.2172/7343826.
- Pastore, G., Swiler, L.P., Hales, J.D., Novascone, S.R., Perez, D.M., Spencer, B.W., Luzzi, L., Van Uffelen, P., Williamson, R.L., 2015. Uncertainty and sensitivity analysis of fission gas behavior in engineering-scale fuel modeling. J. Nucl. Mater. 456, 398–408.
- Pizzocri, D., Rabiti, C., Luzzi, L., Barani, T., Van Uffelen, P., Pastore, G., 2016. Polypole-1: an accurate numerical algorithm for intra-granular fission gas release. J. Nucl. Mater. 478 (5), 333–342.
- Rashid, Y.R., 1974. Mathematical modeling and analysis of fuel rods. Nucl. Eng. Des. 29 (1), 22–32.
- Y. Rashid, R. Dunham, R. Montgomery, Fuel analysis and licensing code: FALCON MOD01, Technical Report EPRI 1011308, Electric Power Research Institute, December 2004.
- Rausch, W N, & Panisko, F E. ANS54: a computer subroutine for predicting fission gas release. United States. doi:10.2172/5495268.
- Ropp, D.L., Shadid, J.N., Ober, C.C., 2004. Studies of the accuracy of time integration methods for reaction-diffusion equations. J. Comput. Phys. 194 (2), 544–574.
- A.M. Ross, R.L. Stoute, Heat transfer coefficient between UO₂ and Zircaloy-2. Technical Report AECL-1552, Atomic Energy of Canada Limited, 1962.
- Ruzickova, M., Vojacek, A., Schulenberg, T., Visser, D. C., Novotny, R., Kiss, A., Maraczy, C., and Toivonen, A. (December 9, 2015). “European Project “Supercritical Water Reactor-Fuel Qualification Test”: Overview, Results, Lessons Learned, and Future Outlook.” ASME. ASME J Nuclear Rad Sci. January 2016; 2(1): 011002. <https://doi.org/10.1115/1.4031034>.
- Spencer, B.W., Williamson, R.L., Stafford, D.S., et al., 2016. 3d modeling of missing pellet surface defects in bwr fuel. Nucl. Eng. Des. 307, 155–171.

- Toptan, A., Hales, J.D., Williamson, R.L., Novascone, S.R., Pastore, G., Kropaczek, D.J., 2020. Modeling of gap conductance for lwr fuel rods applied in the bison code. *J. Nucl. Technol.* 1, 1–12.
- Van Uffelen, A.P., et al., 2019. A review of fuel performance modelling. *J. Nucl. Mater.* 516, 373–412.
- Vojacek, A., Ruizickova, M., and Schulenberg, T. (December 9, 2015). “Design of an In-Pile SCWR Fuel Qualification Test Loop.” ASME. ASME J of Nuclear Rad Sci. January 2016; 2(1): 011003. <https://doi.org/10.1115/1.4030872>.
- White, R.J., Tucker, M.O., 1983. A new fission-gas release model. *J. Nucl. Mater.* 118 (1), 1–38.
- Williamson, R.L., Hales, J.D., Novascone, S.R., Tonks, M.R., Gaston, D.R., Permann, C.J., et al., 2012. Multidimensional multiphysics simulation of nuclear fuel behavior. *J. Nucl. Mater.* 423 (1–3), 149–163.